

# AeroVerse-SatAgent: UAV-Satellite Collaborative Spatial Reasoning Inspired by the Dual Visual Pathway Theory of Cognitive Neuroscience

Wenyi Zhang, Fanglong Yao, *Member, IEEE*, Youzhi Liu, Peng Hu, Zhengqiu Zhu, Chen Gao, Xian Sun, *Senior Member, IEEE*, Kun Fu, *Senior Member, IEEE*

**Abstract**—With the rapid advancement of aerospace embodied intelligence, enabling Unmanned Aerial Vehicles (UAVs) to autonomously understand and reason about complex environments has become increasingly important. However, existing UAV-based spatial reasoning approaches face critical limitations: single-view perception renders them vulnerable to occlusions and perspective distortions, while most VLMs lack explicit geometric modeling, relying on semantic cues and yielding inconsistent reasoning under viewpoint and scale variations. To address these challenges, we propose SatAgent, a UAV-Satellite collaborative spatial reasoning model inspired by the dual-pathway mechanism of the human visual system. By jointly leveraging satellite and UAV perspectives, SatAgent enables robust, accurate reasoning in complex urban environments. We first introduce a Geometric-Aware 3D Reconstruction Encoder that elevates 2D UAV features into explicit 3D spatial representations. Next, we design a multi-view topology-semantic alignment module integrating cross-view features within a unified BEV coordinate system. We further introduce a multi-view consistency loss encouraging viewpoint-invariant representations. Finally, we construct SatAgent-SR130K, the first large-scale UAV-Satellite collaborative multi-view spatial reasoning dataset. Experiments show SatAgent outperforms state-of-the-art general-purpose foundation models and specialized spatial reasoning models by 25.91% and 11.69%, respectively, across diverse tasks, achieving particularly high accuracy in complex geometric relationship reasoning.

**Index Terms**—Multi-view Spatial Reasoning, UAV-Satellite Collaboration, Aerospace Embodied Intelligence, Dual Visual Pathway Mechanism

This work is supported by the National Natural Science Foundation of China under Grants 62306302, 62425115 and by the Beijing Natural Science Foundation under Grant L258082.(Corresponding author: Fanglong Yao.)

Wenyi Zhang, Youzhi Liu, Xian Sun, Kun Fu are with the Aerospace Information Research Institute, Chinese Academy of Sciences, Beijing 100190, China, and also with the University of Chinese Academy of Sciences, Beijing 100190, China, and with the School of Electronic, Electrical and Communication Engineering, University of Chinese Academy of Sciences, Beijing 100190, China, and with the Key Laboratory of Target Cognition and Application Technology (TCAT), Aerospace Information Research Institute, Chinese Academy of Sciences, Beijing 100190, China (e-mail: zhangwenyi24@mails.ucas.ac.cn; liuyouzhi22@mails.ucas.ac.cn; sunxian@aircas.ac.cn; kunfu@ucas.ac.cn).

Fanglong Yao is with the Aerospace Information Research Institute, Chinese Academy of Sciences, Beijing 100190, China, and with the Key Laboratory of Target Cognition and Application Technology (TCAT), Aerospace Information Research Institute, Chinese Academy of Sciences, Beijing 100190, China (e-mail: yaofanglong17@mails.ucas.ac.cn).

Peng Hu is with the School of Computer Science and Engineering, Beihang University, Beijing 100191, China (e-mail: Misaka\_x86@buaa.edu.cn).

Zhengqiu Zhu is with the National Key Laboratory of Digital Intelligent Modeling and Simulation, National University of Defense Technology, Changsha 410073, Hunan Province, China (e-mail: zhuzhengqiu12@nudt.edu.cn).

Chen Gao is with the Beijing National Research Center for Information Science and Technology (BNRist), Tsinghua University, Beijing, China (e-mail: chgao96@gmail.com).

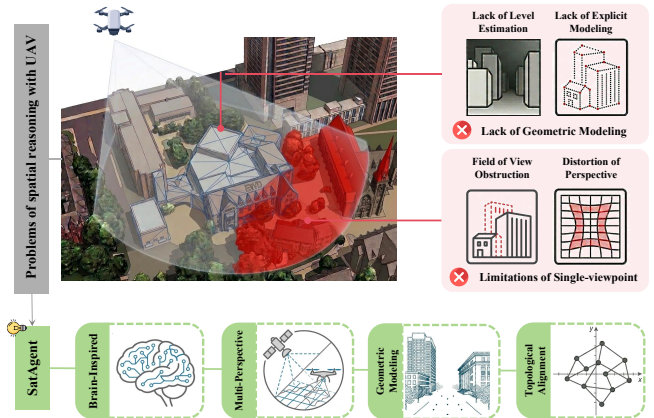


Fig. 1. Two principal limitations of mainstream UAV spatial reasoning: limitations of single-perspective perception and insufficient spatial geometric structure modeling.

## I. INTRODUCTION

**A**EROSPACE embodied intelligence refers to the embedding of perception, cognition, and decision-making capabilities into physical platforms such as satellites and UAVs, enabling autonomous understanding of and intelligent interaction with complex spatial environments [1]–[3]. Among these, UAVs, as representative low-altitude embodied agents, play an increasingly important role in urban sensing, disaster response, autonomous inspection, and environmental monitoring [4]–[8]. A prerequisite for effectively accomplishing these tasks is that UAVs possess reliable reasoning capabilities over the spatial structures and geometric relationships present in the environment, including the relative positions of buildings, vertical hierarchies, occlusion relationships, and traversable path identification [9], [10]. However, real-world scenarios are typically characterized by large spatial scales, complex structures, and drastic viewpoint variations; relying solely on conventional geometric rules or single UAV-perspective inputs is insufficient to meet the spatial understanding demands of complex tasks.

In recent years, researchers have explored UAV spatial reasoning from multiple directions, including geometric reconstruction, depth perception, and end-to-end decision-making [11]–[18], achieving notable progress. Nevertheless, these methods still fall short of the requirements for high-accuracy spatial reasoning in complex urban scenes, primarily exhibit-

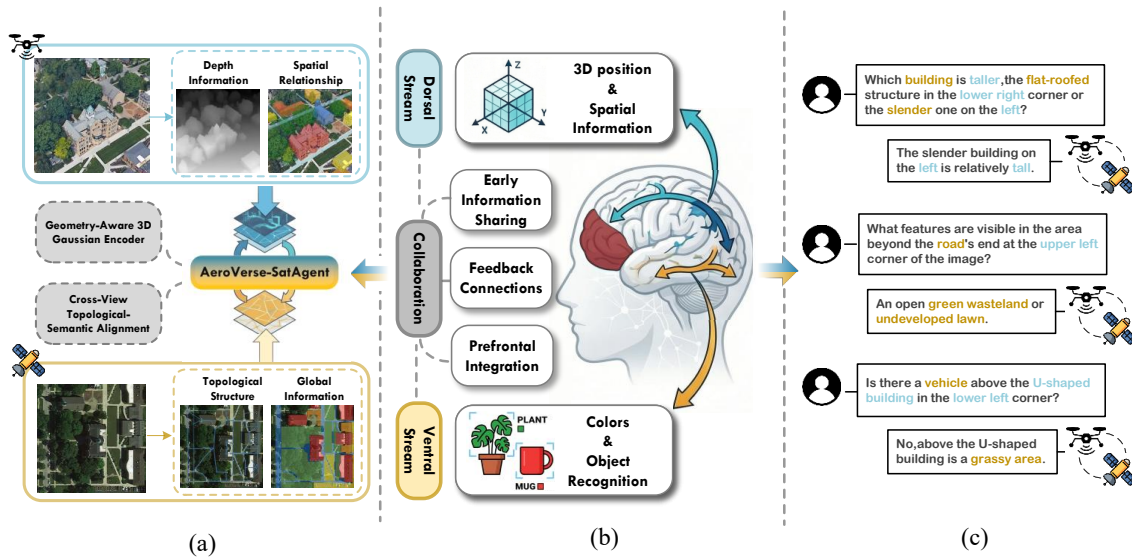


Fig. 2. (a) SatAgent jointly leverages the satellite perspective (global semantic priors) and UAV perspective (local geometric depth) via functionally complementary dual-branch processing. (b) The human dual visual pathway: the ventral pathway handles semantic understanding; the dorsal pathway handles spatial geometry; the two interact bidirectionally. (c) Representative SatAgent-SR130K VQA examples requiring UAV-Satellite collaboration for correct spatial inference.

ing the following two limitations, as illustrated in Fig. 1:

- Limitations of Single-Perspective Perception:** Complex urban environments exhibit pronounced three-dimensional structure and substantial scale variation. Under a single UAV perspective, occlusion, perspective distortion, and depth aliasing are pervasive, forcing the model to simultaneously perform object recognition and spatial relationship reasoning under limited observational conditions, thereby leading to error accumulation. [19]–[22].
- Insufficient Spatial Geometric Structure Modeling:** Existing methods predominantly rely on visual language models for high-level semantic reasoning, but lack explicit modeling of depth, hierarchical structure, and geometric configuration. Spatial relationships are often inferred indirectly through statistical correlations or empirical priors, which tends to fail under viewpoint or scale changes, limiting the geometric consistency and transferability of the reasoning results [21], [23]–[26].

From the perspective of cognitive neuroscience, the remarkable spatial cognitive capabilities of humans do not originate from a single perceptual channel, but rather rely on a multi-pathway cooperative information processing mechanism. The classical dual visual pathway theory [27]–[29] posits that the human visual system comprises the ventral pathway and the dorsal pathway: as illustrated in Fig. 2(b), the ventral pathway is primarily responsible for object recognition, categorical discrimination, and semantic comprehension, whereas the dorsal pathway focuses on spatial localization, geometric relationships, depth perception, and action-guidance-related information processing. These two visual pathways form a tightly coupled collaboration through multilevel bidirectional information exchange. The object recognition and semantic features extracted by the ventral pathway serve as target

anchors for the spatial localization performed by the dorsal pathway, while the spatial positions and motion trajectories resolved by the dorsal pathway in turn constrain the object segmentation boundaries of the ventral pathway. The two pathways achieve dynamic integration of semantic understanding and spatial reasoning through the interconnections between the parietal and temporal cortices.

Inspired by the human dual visual pathway mechanism, this paper proposes SatAgent, a UAV-Satellite collaborative multi-view spatial reasoning model. As illustrated in Fig. 2(a), SatAgent achieves multi-level spatial understanding by jointly leveraging two complementary perspectives. The satellite view provides stable top-down global observations suited for characterizing regional layout, topological structure, and relative positional relationships, functionally corresponding to the ventral pathway. The UAV view captures rich local geometry, vertical structure, and depth information through oblique close-range observations, functionally corresponding to the dorsal pathway. Mirroring the coordinated ventral–dorsal mechanism, SatAgent maps global semantic priors from the satellite perspective and 3D geometric cues from the UAV perspective into a shared coordinate system for joint alignment, yielding viewpoint-invariant and scale-consistent spatial representations through structure-aware multi-view relational modeling.

SatAgent introduces three key components: a Dual-Channel Collaborative Encoder, a Geometric-Aware 3D Reconstruction Encoder, and a Multi-view Topology-Semantic Alignment Module. Critically, functional separation between the semantic and geometric branches prevents the two encoders from collapsing into redundant representations—a common failure mode when heterogeneous visual inputs share a single feature extractor—while bidirectional cross-stream interaction ensures that each branch is guided by complementary cues rather than optimizing in isolation. The reconstruction encoder further

reduces the perspective distortion artifacts inherent in single-view depth reasoning by grounding UAV features in an explicit metric BEV coordinate system aligned with the satellite view, improving cross-view spatial correspondence. The alignment module then replaces naive feature concatenation with structured graph propagation, which captures non-local topological dependencies that convolution-based fusion consistently fails to model. Coupled with a multi-view consistency loss providing explicit gradient supervision across answer generation, structural alignment, and pathway specialization, the model consistently improves generalization on tasks requiring metric and topological perception.

To support the above research model, this paper constructs SatAgent-SR130K, the visual question answering dataset specifically designed for UAV-Satellite spatial reasoning. Built upon GeoText-1652 [30], which provides geo-referenced scene images with regional descriptions and bounding box annotations but no question-answer pairs, we introduce 130K spatial reasoning QA annotations from scratch spanning eight reasoning categories. Beyond scale, we enforce a single-view unsolvability principle ensuring that cross-view questions cannot be resolved from either perspective alone, requiring genuine multi-view collaborative inference rather than single-perspective shortcuts. We further address a systematic ambiguity absent from the original dataset: all directional references are unified under the satellite image coordinate system and annotated via a machine-readable `direction_frame` field, eliminating semantic inconsistencies caused by varying UAV shooting angles.

In summary, the main contributions of this paper are as follows:

(1) We propose SatAgent, a UAV-Satellite collaborative spatial reasoning model inspired by the dual visual pathway mechanism, featuring a Dual-Channel Collaborative Encoder that separates semantic and geometric processing via bidirectional cross-stream gating between the satellite and UAV branches, establishing a functionally complementary representational foundation for cross-view spatial reasoning.

(2) We construct SatAgent-SR130K, the first large-scale UAV-Satellite collaborative spatial reasoning dataset, comprising 130K QA annotations across geo-referenced scenes and eight structural reasoning categories.

(3) We propose a Geometric-Aware 3D Reconstruction Encoder that lifts UAV features into metric BEV space via covariance-aware 3D Gaussian soft projection and affine alignment to the satellite coordinate system, eliminating perspective distortion artifacts inherent in single-view depth reasoning.

(4) We propose a Multi-view Topology-Semantic Alignment Module employing dynamic  $k$ -NN graph attention to model cross-view topological dependencies, and cross-view gating to adaptively balance satellite semantic and UAV geometric feature contributions, enabling structured non-local spatial relationship modeling beyond naive feature concatenation.

(5) We propose a multi-view consistency loss providing explicit gradient supervision across three levels: answer generation ( $\mathcal{L}_{\text{im}}$ ), cross-view structural alignment ( $\mathcal{L}_{\text{topo}}$ ,  $\mathcal{L}_{\text{con}}$ ), and dual-pathway functional differentiation ( $\mathcal{L}_{\text{geo}}$ ,  $\mathcal{L}_{\text{div}}$ ), ensuring

that the ventral–dorsal functional separation is driven by explicit training signals rather than implicit emergence.

## II. RELATED WORK

### A. Spatial Reasoning via Large Language Models

In recent years, multimodal large language models (MLLMs) have achieved remarkable progress on 2D visual tasks yet continue to face significant challenges in complex 3D spatial reasoning, including metric distance estimation and 3D bounding box localization [22], [42]–[45]. Early work sought to reconstruct 3D scenes from multi-view images or point clouds: 3D-LLM [46] and LLaVA-3D [47] inject the physical world into language models via 3D point cloud features, but at the cost of substantial computational resources that limit scalability. ConceptGraphs [48] reduces this overhead by constructing 3D scene graphs rather than processing raw 3D data directly. A parallel line develops region-level VLMs to handle complex local spatial relationships: KOSMOS-2 [49], Shikra [50], and Ferret [51] achieve region-level understanding via bounding boxes or masks, while RegionGPT [52] and Osprey [53] extend this to pixel-level features supporting reasoning over arbitrarily shaped regions. More recently, approaches enhancing 2D models through monocular depth estimation have gained traction: SpatialVLM [54] directly comprehends spatial relationships and metric distances; SpatialRGPT [22] integrates monocular depth into existing visual encoders, substantially improving directional and distance perception, yet its spatial representations are still fed into the LLM in textual or symbolic form, compromising accuracy under complex geometric configurations.

These explorations reveal a fundamental tension: a single perspective cannot simultaneously achieve precise perception of both global topology and local geometry. *Motivated by this insight, SatAgent exploits the complementary advantages of satellite and UAV perspectives, constructing viewpoint-invariant spatial representations through explicit geometric modeling within a unified coordinate system, endowing LLMs with metric perception capabilities grounded in the physical world.*

### B. Multi-view Spatial Reasoning

Integrating collaborative spatial reasoning from multiple views has emerged as a key pathway to overcoming the limitation of single-perspective approaches. Feature-alignment methods such as UCDNet [55] and DHD [56] achieve UAV-Satellite correspondence via unsupervised domain adaptation and knowledge distillation, respectively, but their outputs remain confined to classification labels without spatial reasoning expressed in natural language. Graph-based methods such as ConceptGraphs [48] construct unified 3D semantic graphs from multi-view fusion, yet lack end-to-end learning for viewpoint-invariant spatial relationships. Multi-image VLMs—MANTIS [57] and LLaVA-NeXT-Interleave [58]—process multiple visual inputs jointly but rely on implicit spatial representations. Video-3D LLM [59] treats video as a multi-view sequence but degrades under drastic viewpoint changes. BEVFormer [60] learns unified BEV representations

TABLE I

COMPARISON OF REPRESENTATIVE UAV-SATELLITE SPATIAL REASONING BENCHMARKS. **C-V Q.**: DEDICATED CROSS-VIEW QUESTION SPLIT REQUIRING BOTH VIEWS FOR CORRECT INFERENCE; **STRUCT. GEO.**: INCLUDES DEDICATED STRUCTURAL GEOMETRIC REASONING CATEGORIES (E.G., DEPTH ORDERING, HEIGHT-FOOTPRINT CONSISTENCY, OCCLUSION COMPLETION, PATH REACHABILITY); **PED.**: PEDESTRIAN, **VEH.**: VEHICLE, **SAT.**: SATELLITE, **TEM.**: TEMPLATES;  $\checkmark$  = FULLY SUPPORTED, *part.* = PARTIALLY SUPPORTED,  $\times$  = NOT SUPPORTED;  $\dagger$  APPROXIMATE VALUE.

Benchmark	Year	Platform	Input	Environment	QA Num.	Tasks	Annotation	C-V Q.	Struct. Geo.
<i>General Multi-view Benchmarks</i>									
VSI-Bench [31]	2025	Egocentric Camera	Video	Indoor	$\sim$ 5K	8	Human	$\times$	<i>part.</i>
ViewSpatial-Bench [32]	2025	Multi-camera	Image	Indoor + Outdoor	$\sim$ 5.7K	5	Rules+Tem.	<i>part.</i>	$\times$
MM-Spatial [33]	2025	RGB-D Camera	Image	Indoor	–	–	Rules+Tem.	$\times$	<i>part.</i>
MMSI-Bench [34]	2025	Multi-camera	Image	Indoor + Outdoor	1K	11	Human	$\checkmark$	<i>part.</i>
UrBench [35]	2025	Street+Sat.	Image	Urban Outdoor	11.6K	14	Rules+LLM+Human	<i>part.</i>	$\times$
All-Angles Bench [36]	2025	Ego+Exo Camera	Image	Indoor + Outdoor	2.1K	6	Human	$\checkmark$	$\times$
<i>Aerial Multi-view Benchmarks</i>									
AirCopBench [37]	2026	Multi-UAV	Image	Urban Aerial	14.6K	14	Rules+LLM+Human	<i>part.</i>	$\times$
CityCube [38]	2026	Ped.+Veh.+UAV+Sat.	Image	Aerial + Street	5K	59	Tem.+LLM+Human	<i>part.</i>	<i>part.</i>
Open3D-VQA [39]	2025	UAV	Image	Outdoor Aerial	73K	7	Rules+Tem.	$\times$	<i>part.</i>
UAVReason [40]	2026	UAV	Image	Outdoor Aerial	273K	22	Rules+LLM	$\times$	<i>part.</i>
LinkS <sup>2</sup> Bench [41]	2026	UAV+Sat.	Video	Outdoor Aerial	17.9K	12	LLM+Human	$\checkmark$	<i>part.</i>
<b>SatAgent-SR130K (Ours)</b>	2026	UAV+Sat.	<b>Image</b>	<b>Urban Aerial</b>	<b>130K</b>	<b>8</b>	<b>Tem.+LLM+Human</b>	$\checkmark$	$\checkmark$

from multi-camera inputs via spatiotemporal grid queries, yet without language-grounded spatial reasoning capability. MM-Spatial [33] demonstrates that explicit depth augmentation substantially improves 3D spatial perception, yet its design targets indoor small-scale scenes and cannot accommodate the extreme scale disparities between satellite orthographic and UAV oblique imagery. *In response to these limitations, this paper designs a Geometric-Aware 3D Reconstruction Encoder and a Multi-view Topology-Semantic Alignment Module, achieving truly geometrically consistent multi-view collaborative reasoning.*

Despite these advances, dedicated benchmarks for cross-view aerial spatial reasoning remain scarce, as summarized in Table I. General multi-view benchmarks—VSI-Bench [31], ViewSpatial-Bench [32], MM-Spatial [33], and MMSI-Bench [34]—are confined to indoor or mixed-scene settings and lack aerial-specific geometric reasoning tasks. Among aerial benchmarks, AirCopBench [37] advances multi-UAV collaborative perception without global satellite references. CityCube [38] spans multiple platforms including satellites but does not enforce single-view unsolvability, allowing single-perspective shortcuts. Most closely related, LinkS<sup>2</sup>Bench [41] addresses dynamic UAV-satellite cross-view reasoning but focuses on temporal anchoring via video rather than static structural spatial categories. *SatAgent-SR130K fills this gap with 130K QA pairs across eight structural reasoning categories under strict single-view unsolvability constraints.*

### C. Aerial and Remote Sensing Visual Understanding

Research in aerial and remote sensing visual understanding has broadly advanced along two lines. Early work focused on constructing visual question answering benchmarks for remote sensing imagery: RSVQA [61] pioneered the introduction of the VQA paradigm into the remote sensing domain, covering basic question types such as existence, quantity, and comparison; however, constrained by template-based generation, it

exhibits insufficient semantic diversity, with reasoning depth limited primarily to object-level attribute judgment rather than scene-level spatial relationships. DIOR-RSVG [62] and EarthVQA [63] further incorporate region-level referring expressions and multi-category spatial relationships, providing important benchmarks for fine-grained remote sensing visual understanding evaluation. STAR [64] provides the first scene graph generation benchmark over large-size satellite imagery, yet covers only single-perspective spatial relations. The second line is dedicated to transferring large-scale pre-trained visual language models to remote sensing scenarios: RemoteCLIP [65] substantially improves zero-shot retrieval and classification on remote sensing imagery through continual pre-training on large-scale remote sensing image-text pairs; GeoChat [66] introduces remote sensing-specific instruction fine-tuning datasets, greatly improving the performance of general MLLMs on scene understanding, object detection, and change detection tasks; SkyEyeGPT [67] incorporates multiple remote sensing visual language tasks into a single model through a unified instruction format, preliminarily exploring cross-task transfer capabilities. However, all of the above works lack systematic exploitation of multi-view collaborative information. To address this gap, University-1652 [68] and GeoText-1652 [30] have established geo-referenced image datasets from satellite, UAV, and ground-level tri-perspectives, providing an important data foundation for cross-view geo-localization and natural language-guided UAV navigation. *Building upon these foundations, this paper constructs SatAgent-SR130K, and proposes the corresponding UAV-Satellite reasoning model SatAgent, filling a critical gap in the progression from single-perspective perception to multi-view collaborative reasoning in remote sensing visual understanding.*

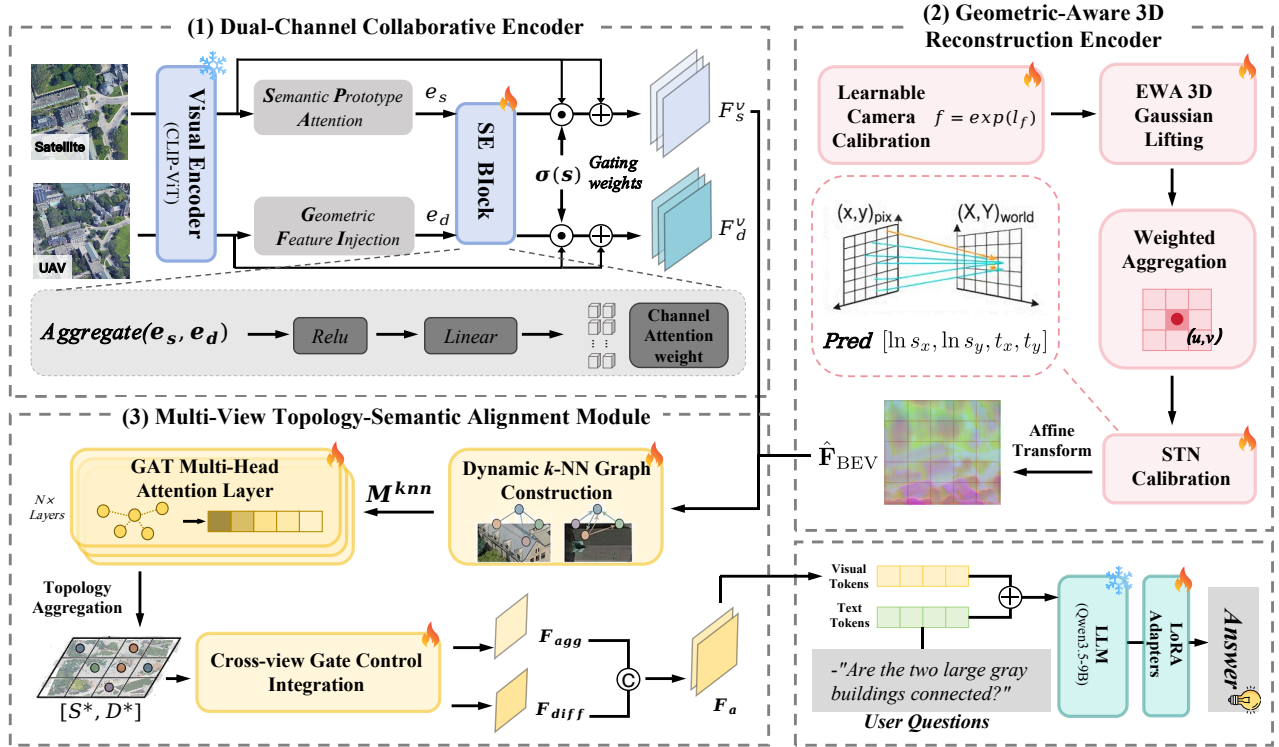


Fig. 3. **Overall architecture of the SatAgent.** The model consists of three core modules working in concert: (1) **Dual-Channel Collaborative Encoder:** Inspired by the human dual visual pathways, it models complementary spatial information through a semantic prototype pathway and a geometric feature injection pathway, and implements bidirectional information feedback via bidirectional cross-stream gating; (2) **Geometric-Aware 3D Reconstruction Encoder:** Utilizes learnable camera calibration to guide EWA 3D Gaussian Lifting, soft-projecting UAV-view features into BEV space, and achieves coordinate alignment at the physical scale via STN affine transformation; (3) **Multi-view Topology-Semantic Alignment Module:** Captures cross-view topological dependencies based on feature semantic similarity via a dynamic  $k$ -NN graph and a graph attention network (GAT), and adaptively balances satellite semantic and UAV geometric features via cross-view gating. Finally, the aligned visual tokens and the question are jointly input into a LLM for geometry-aware enhanced spatial reasoning and answer generation.

### III. METHOD

This section systematically describes the methodological details of the SatAgent model. §III-A presents the overall architecture and data flow; §III-B introduces the Dual-Channel Collaborative Encoder; §III-C describes the Geometric-Aware 3D Reconstruction Encoder; §III-D elaborates the Multi-View Topology-Semantic Alignment Module; §III-E presents the LLM inference and parameter-efficient fine-tuning; §III-F details the multi-view consistency loss function design.

#### A. SatAgent Architecture

Inspired by the Dual Visual Streams of the human visual system, SatAgent jointly leverages satellite imagery (providing global topological and semantic priors) and UAV imagery (capturing local three-dimensional geometry and depth information), achieving UAV-Satellite collaborative spatial reasoning through a functionally complementary dual-branch feature processing pipeline. The overall architecture is illustrated in Fig. 3.

**Overall Pipeline.** The model sequentially executes the following core stages: (1) **Dual-Channel Collaborative Encoder:** Both satellite and UAV images extract initial features through a frozen CLIP ViT-B/16 [69] encoder, which are then processed by specialized adapters configured independently for each

branch—the satellite branch, enriched with semantic information, is better suited for region category discrimination, while the UAV branch, enhanced with geometric injection, is more sensitive to depth structure. The two branches form a synergistic mechanism of semantic anchoring and geometric constraint through bidirectional gating interaction. (2) **Geometric-Aware 3D Reconstruction Encoder** (§III-C): UAV features are back-projected using a learnable focal length, soft-projected via covariance-aware Gaussian lifting, and affine-calibrated across views, ultimately achieving spatially meaningful correspondence with satellite features within a unified bird’s-eye view (BEV) coordinate system. (3) **Multi-view Topology-Semantic Alignment Module** (§III-D): The aligned dual-branch features are structure-aware fused via dynamic  $k$ -NN graph convolution, converted into visual tokens, and fed into the large language model to complete spatial question answering. During training, a multi-objective loss jointly constrains the model across three levels—language modeling, structural alignment, and pathway functional separation (§III-F). (4) **LLM Inference** (§III-E): The aligned visual tokens and the question are jointly input into a large language model (LLM) for geometry-aware enhanced spatial reasoning and answer generation.

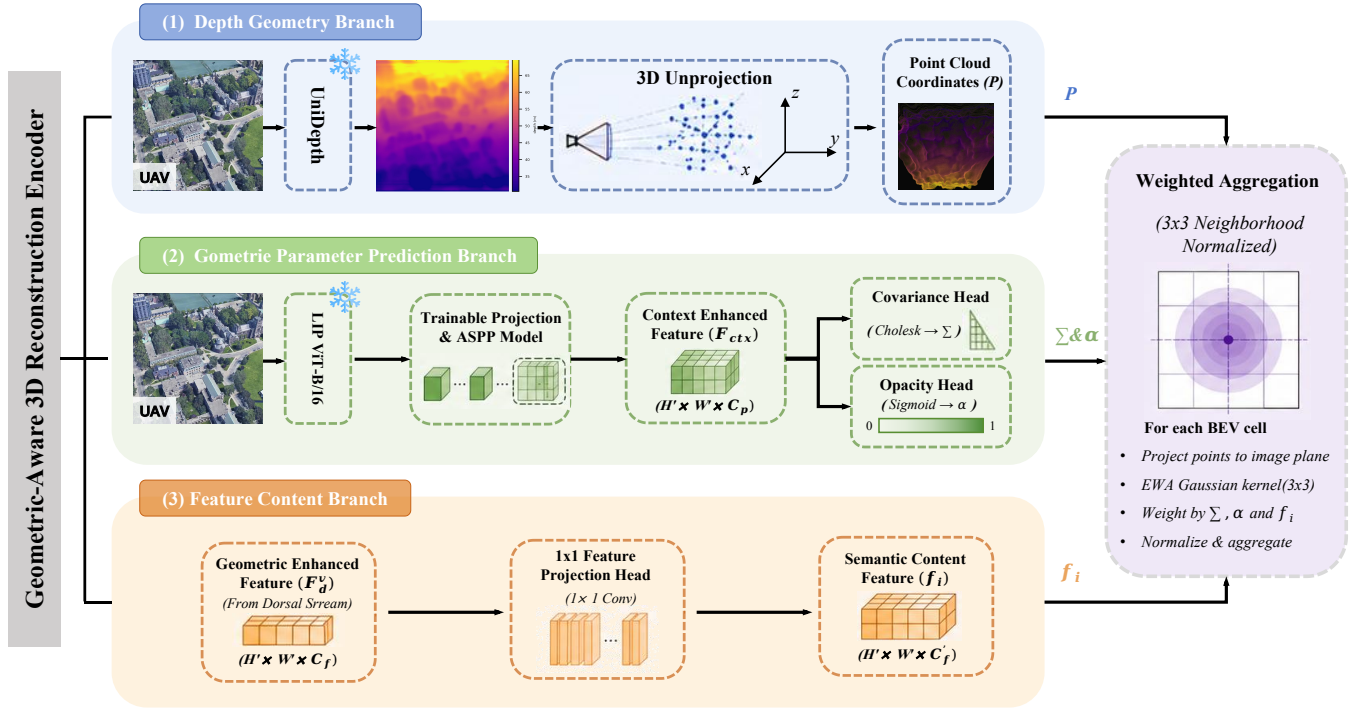


Fig. 4. Data flow of the Geometric-Aware 3D Reconstruction Encoder. Three inputs converge in EWA Gaussian soft projection: the Depth-Geometry Branch supplies metric 3D point clouds via frozen UniDepth and a learnable focal calibrator; the Geometric Parameter Prediction Branch predicts per-pixel Choleski covariance and opacity via ASPP; and the Feature Content Input feeds dorsal stream output  $\mathbf{F}_d^v$  as the semantic payload. Weighted aggregation produces  $\mathbf{F}_{\text{BEV}}$ , subsequently aligned to the satellite coordinate system via STN affine calibration.

## B. Dual-Channel Collaborative Encoder

We design the Dual-Channel Collaborative Encoder to address the heterogeneity of semantic and geometric features in multi-view imagery: it extracts semantic prototypes from the satellite view via a Ventral Pathway Adapter, injects depth-gradient geometry from the UAV view via a Dorsal Pathway Adapter, and couples the two via bidirectional gating, establishing a representation that is both semantically discriminative and geometrically aware.

1) *Ventral Pathway Adapter*: To make satellite features better discriminate semantic categories rather than encode local geometry—mirroring the Ventral Stream’s role in object recognition [28], [29]—we design a Semantic Prototype Attention (SPA) module that maintains  $K$  learnable prototype vectors, simulating category-selective responses in inferotemporal cortex. The input features activate the most relevant prototypes via multi-head cross-attention, and the mean response  $\bar{a}_k$  of each prototype aggregates a scene-level semantic embedding

$$\mathbf{e}_s = \ell_2 \left( \sum_{k=1}^K \bar{a}_k \mathbf{p}_k \right), \quad (1)$$

where  $\mathbf{p}_k$  is the  $k$ -th prototype.  $\mathbf{e}_s$  then conditions a channel gate that imposes a semantic directional bias on the satellite features, while a depth-wise low-pass convolution suppresses high-frequency geometric noise, reflecting the ventral pathway’s relative insensitivity to fine spatial detail. The output is the semantically enhanced feature  $\mathbf{F}_s^\delta$ .

2) *Dorsal Pathway Adapter*: To let the UAV branch perceive depth hierarchy and 3D structure rather than

CLIP’s semantic-texture features—corresponding to the Dorsal Stream’s role in depth and spatial relations—we design a geometric feature injection mechanism. From the existing UniDepth [70] depth map, fixed Sobel/Laplacian operators extract a 6-channel geometric descriptor combining depth, normalized surface-gradient directions ( $\hat{g}_x, \hat{g}_y$ ), gradient magnitude  $\hat{m}$ , curvature  $\tanh(\nabla^2 D)$ , and the interaction term  $D \odot \hat{m}$ :

$$\mathbf{G} = [D, \hat{g}_x, \hat{g}_y, \hat{m}, \tanh(\nabla^2 D), D \odot \hat{m}]. \quad (2)$$

$\mathbf{G}$  is fused with CLIP features through learnable gating after lightweight projection, and supplemented with a depth-sensitive spatial attention conditioned on gradient magnitude, enhancing responses at object boundaries and depth discontinuities. The output is the geometrically enhanced feature  $\mathbf{F}_d^\delta$ , together with a distilled global geometric embedding  $\mathbf{e}_d$ .

3) *Bidirectional Cross-Stream Gating*: Inspired by the dorsal–ventral feedback formed through parietal–temporal interconnections, the two adapters’ outputs ( $\mathbf{F}_s^\delta, \mathbf{e}_s$  and  $\mathbf{F}_d^\delta, \mathbf{e}_d$ ) are coupled by a bidirectional residual modulation. First, in the ventral→dorsal direction,  $\mathbf{e}_s$  is mapped via SE attention [71] into channel weights for the UAV features, sharpening geometric responses in semantically salient regions (e.g., rooftops, intersections); then, in the dorsal→ventral direction,  $\mathbf{e}_d$  correspondingly modulates the satellite features, using 3D cues to constrain semantic activations and prevent appearance-only misattribution. Both modulations are applied residually:

$$\begin{aligned} \mathbf{F}_d^v &= \mathbf{F}_d^\delta \odot (1 + \sigma(s_{v \rightarrow d}) \cdot \text{SE}(\mathbf{e}_s)), \\ \mathbf{F}_s^v &= \mathbf{F}_s^\delta \odot (1 + \sigma(s_{d \rightarrow v}) \cdot \text{SE}(\mathbf{e}_d)), \end{aligned} \quad (3)$$

where  $\text{SE}(\cdot)$  compresses the embedding to  $C/4$  dimensions before restoring  $C$  channel weights, and  $s_{v \rightarrow d}, s_{d \rightarrow v} \in \mathbb{R}$  are gating strengths initialized to 0. After gating,  $\mathbf{F}_d^v$  flows into the Geometric-Aware 3D Reconstruction Encoder (§III-C), while  $\mathbf{F}_s^v$  flows directly into the satellite feature pathway for cross-view alignment (§III-D), enabling geometry-aware BEV projection and semantics-aware alignment, respectively. The residual form keeps network behavior at initialization equivalent to the ungated case; training then lets gradients adaptively determine each direction’s activation, yielding functional complementarity rather than forced symmetry.

### C. Geometric-Aware 3D Reconstruction Encoder

Inspired by the dorsal stream’s role in reconstructing 2D retinal projections into metric 3D scene representations [27], [28], and following the design philosophy of BEVFusion [72], this encoder combines learnable camera calibration with 3D Gaussian lifting to map UAV features into a depth-aware BEV representation, eliminating the perspective gap with satellite imagery (Fig. 4).

1) *Depth-Geometry Branch and Geometric Parameter Prediction*: Two parallel branches first prepare, for each pixel  $i$ , the geometric primitives needed for Gaussian lifting. The **Depth-Geometry Branch** uses a frozen UniDepth [70] depth map  $\mathbf{D}$  together with a learnable equivalent focal length  $f = \exp(\ell_f)$  and trainable principal-point offsets  $(\delta_x, \delta_y)$  to back-project each pixel  $(u, v, d)$  to

$$X = \frac{(u - c_x + \delta_x) \cdot d}{f}, Y = \frac{(v - c_y + \delta_y) \cdot d}{f}, Z = d, \quad (4)$$

yielding  $\mathbf{xyz} \in \mathbb{R}^{B \times 3 \times H_f \times W_f}$ , whose  $(X, Y)$  define the BEV location  $(u_i, v_i)$  used below. In parallel, the **Geometric Parameter Prediction Branch** passes the CLIP feature map through an ASPP module to obtain  $\tilde{\mathbf{F}}$ , from which a covariance head regresses the Cholesky factor of a positive-definite matrix,

$$\Sigma_i = \mathbf{L}_i \mathbf{L}_i^\top, \quad (\mathbf{L}_i)_{jk} = \begin{cases} \exp(l_{jk}), & j = k \\ l_{jk}, & j > k, \end{cases} \quad (5)$$

while an opacity head outputs  $\alpha_i \in (0, 1)$ . The exponential diagonal guarantees  $\Sigma_i \succ 0$  without the degenerate solutions of direct covariance prediction. Together with the dorsal-stream feature  $\mathbf{F}_d^v$  (the Feature Content Input in Fig. 4), the quadruple  $(\mathbf{xyz}_i, \Sigma_i, \alpha_i, \mathbf{f}_i)$  fully specifies the 3D Gaussian element at pixel  $i$ .

2) *Covariance-Aware Gaussian Soft Projection*: To let these Gaussian elements genuinely shape the BEV features, we replace count-normalized hard scatter with an EWA (Elliptical Weighted Average)-style soft projection [73]. The contribution of pixel  $i$  to BEV cell  $(u, v)$  is

$$w_{i \rightarrow (u,v)} = \alpha_i \cdot \exp\left(-\frac{(u - u_i)^2}{2\sigma_{b,x}^2(i)} - \frac{(v - v_i)^2}{2\sigma_{b,y}^2(i)}\right), \quad (6)$$

where  $(u_i, v_i)$  comes from Eq. (4) and  $\sigma_{b,x}^2(i), \sigma_{b,y}^2(i)$  are the XY components of  $\Sigma_i$  in BEV pixel units. Features are aggregated by weighted normalization,  $\mathbf{F}_{\text{BEV}}(u, v) = \sum_i w_{i \rightarrow (u,v)} \mathbf{f}_i / (\sum_i w_{i \rightarrow (u,v)} + \varepsilon)$ , within a  $3 \times 3$  window.

This lets pixels with large depth uncertainty form diffuse responses while occluded (low-opacity) pixels are automatically suppressed, fully exploiting the predicted covariance.

3) *Cross-View Affine Calibration*: Even after focal-length calibration, residual scale and offset mismatches between the UAV BEV and the satellite coordinate system persist due to differing ground-sampling distances. We introduce an STN [74]-style module that regresses a 4-DoF transform  $\Theta = [\ln s_x, \ln s_y, t_x, t_y]$  from the globally pooled and concatenated  $\mathbf{F}_s^v$  and  $\mathbf{F}_{\text{BEV}}$  via a two-layer MLP (hidden dim  $C/4$ ). The log-scale parameterization guarantees  $s_x, s_y > 0$ ; rotation is omitted since both views are approximately top-down, and including it would only add optimization difficulty. The calibrated feature is obtained via differentiable bilinear sampling,

$$\hat{\mathbf{F}}_{\text{BEV}} = \mathcal{T}(\mathbf{F}_{\text{BEV}}; \Theta), \quad (7)$$

with the MLP’s final layer zero-initialized for a near-identity start;  $\Theta$  is then optimized jointly by  $\mathcal{L}_{\text{topo}}$  and  $\mathcal{L}_{\text{lm}}$ , without extra geometric supervision. Together with the learnable focal length above, this module constitutes the *BEVScaleCalibrator* evaluated as Variant B1 (§IV-C).

### D. Multi-View Topology-Semantic Alignment Module

When the dual visual pathways converge in prefrontal cortex, a unified “cognitive map” associates ventral semantic prototypes with dorsal spatial coordinates, enabling inference of path connectivity and regional adjacency [28], [29]. After BEV calibration,  $\mathbf{F}_s^v$  and  $\hat{\mathbf{F}}_{\text{BEV}}$  are geometrically aligned but still semantically divergent—satellite features carry global topology and regional attributes, UAV features emphasize local geometry. Since conventional fusion cannot capture nonlinear cross-view relations such as path connectivity, and fixed-topology graphs only aggregate spatially adjacent nodes, we adopt a dynamic  $k$ -NN graph whose topology is built on-the-fly from feature similarity, combined with a graph attention network and cross-view gated fusion (Fig. 5).

1) *Semantically Adaptive Topology Layer*: To encode the prior that semantically similar regions should be preferentially connected, the graph is built dynamically from feature cosine similarity augmented with a learnable spatial-distance bias:

$$a_{ij} = \frac{\mathbf{h}_i^\top \mathbf{h}_j}{\|\mathbf{h}_i\| \|\mathbf{h}_j\|} + \sigma(\gamma_s) \cdot \frac{\mathbf{p}_i^\top \mathbf{p}_j}{\|\mathbf{p}_i\| \|\mathbf{p}_j\|}, \quad (8)$$

where  $\mathbf{h}_i$  is the node feature,  $\mathbf{p}_i$  is a parameter-free 2D sinusoidal positional encoding [75], and  $\sigma(\gamma_s)$  is a learnable spatial decay coefficient. For each node, the  $k=8$  highest-similarity neighbors are kept (others set to  $-\infty$ ), giving a sparse mask  $\mathbf{M}^{\text{knn}}$ , over which GAT [76]-style multi-head attention propagates and updates node features—yielding the topology-propagated satellite and UAV representations  $\mathbf{S}^*$  and  $\mathbf{D}^*$  used below. Positional encoding matters because, after ventral adaptation, two spatially distinct but visually similar regions (e.g., rooftops of different buildings) could otherwise be erroneously connected by semantic similarity alone; positional encoding lets the attention distinguish them.

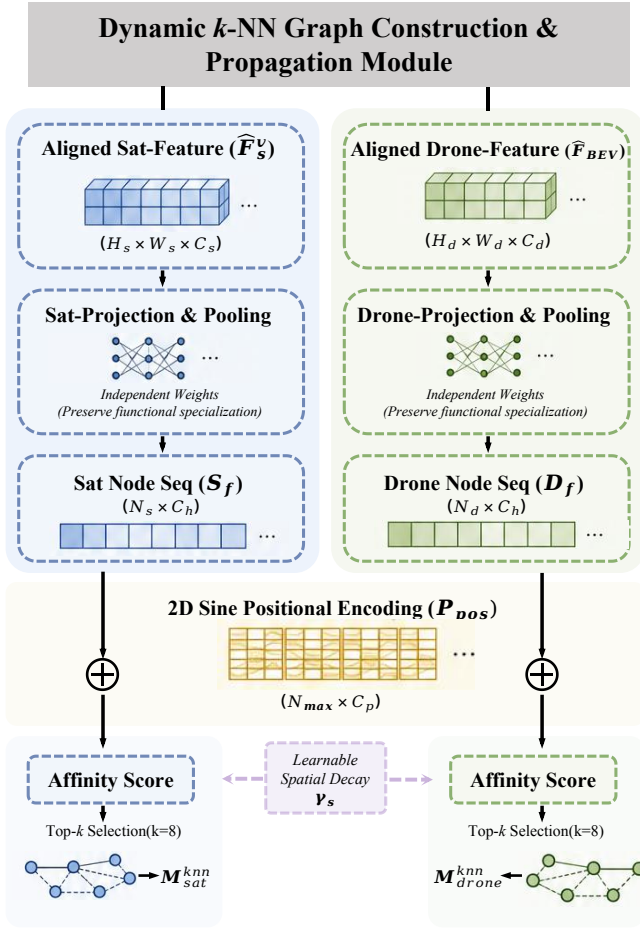


Fig. 5. Data flow of the Dynamic  $k$ -NN Graph Construction and Propagation Module. Satellite features  $\mathbf{F}_s^v$  and drone BEV features  $\hat{\mathbf{F}}_{BEV}$  are independently projected and flattened into node sequences. Edge affinity scores combine feature cosine similarity with learnable spatially-weighted positional encoding, from which the top- $k$  neighbors are retained to form sparse mask  $\mathbf{M}^{knn}$ .

2) *Cross-View Gated Fusion*: To adaptively balance satellite semantic information and UAV geometric information when fusing  $\mathbf{S}^*$  and  $\mathbf{D}^*$ , we replace simple concatenation—which weighs all channels uniformly—with channel-wise gating that learns input-dependent weights emphasizing whichever branch is locally more informative, a principle validated for heterogeneous multimodal fusion by Arevalo et al. [77]. A differential residual term further exposes the complementary discrepancy between branches:

$$\mathbf{F}_a = \text{Conv}_{1 \times 1}(\mathbf{G} \odot \mathbf{S}^* + (1 - \mathbf{G}) \odot \mathbf{D}^*; \mathbf{S}^* - \mathbf{D}^*), \quad (9)$$

where  $\mathbf{G} = \sigma(\mathbf{W}_g[\mathbf{S}^*; \mathbf{D}^*])$  is the channel-wise gate and  $\mathbf{S}^* - \mathbf{D}^*$  supplies a complementary discrepancy signal. The satellite and UAV branches use separate, non-shared projection layers, since their feature distributions have already diverged systematically during the dual-channel adapter stage—sharing weights here would impose unnecessary alignment pressure and negate the gains from functional separation. The resulting  $\mathbf{F}_a$  is the aligned feature passed to the LLM inference stage (§III-E).

### E. LLM Inference and Parameter-Efficient Fine-tuning

To effectively inject the aligned visual representations into the large language model while avoiding catastrophic forgetting of the world knowledge carried by the LLM, we adopt a strategy combining soft token injection with LoRA [78] parameter-efficient fine-tuning.

The aligned feature  $\mathbf{F}_a$  is projected to  $N_v=256$  visual tokens, and prepended to the question text embedding along the sequence dimension as  $[\mathbf{V}; \mathbf{T}]$ . The prepended visual tokens enable the LLM to directly access the global visual context during self-attention computation over text tokens. The LLM backbone (Qwen3.5-9B) is loaded with 4-bit double quantization in NF4 format. LoRA adapters are applied only to the attention projection layers and feed-forward network layers, with rank  $r=16$ , making the number of trainable parameters approximately 1% of the total. During training, labels for question tokens are masked to  $-100$ , ensuring that gradients are back-propagated only from the answer generation stage, preventing the model from memorizing input formats rather than learning visual-text semantic mappings. Structured output constraints are embedded in the prompts according to question category (e.g., yes/no questions or single-word/phrase questions), eliminating the need for constrained decoding on the inference side and maintaining a streamlined and efficient inference pipeline.

### F. Multi-View Consistency Loss Constraints

The dual-pathway collaborative mechanism requires explicit training signals to drive the two-branch features toward functional differentiation. We jointly constrain learning across three levels—answer generation, cross-view structural alignment, and dual-pathway functional differentiation—via the following loss design.

The primary supervision signal is the autoregressive language modeling loss  $\mathcal{L}_{lm}$ , backpropagating gradients only through answer tokens. At the global embedding level, a symmetric InfoNCE contrastive loss [69], [79]  $\mathcal{L}_{con}$  (temperature  $\tau=0.07$ ) drives viewpoint-invariant scene-level representations. We additionally propose the following core losses.

**Position-Aware Structural Consistency Loss.** Standard Gram matrix matching discards spatial position information and becomes invalid under the extreme viewpoint disparity between satellite orthographic and UAV oblique imagery. Instead, we partition the calibrated BEV feature maps  $\mathbf{F}_s^v, \hat{\mathbf{F}}_{BEV}$  uniformly into  $R \times R$  ( $R=4$ ) non-overlapping regions, extract the [mean, std] descriptor  $\mathbf{d}_r^v \in \mathbb{R}^{2C}$  per region, and apply symmetric InfoNCE to the  $\ell_2$ -normalized descriptor matrices  $\hat{\mathbf{D}}_s, \hat{\mathbf{D}}_d \in \mathbb{R}^{(BR^2) \times 2C}$ :

$$\mathcal{L}_{topo} = \frac{1}{2} \left[ \text{CE}(\mathbf{S}, \mathbf{y}) + \text{CE}(\mathbf{S}^\top, \mathbf{y}) \right], \quad (10)$$

where  $\mathbf{S} = \hat{\mathbf{D}}_s \hat{\mathbf{D}}_d^\top / \tau_{topo}$  ( $\tau_{topo}=0.1$ ) and  $\mathbf{y}$  assigns each row its positive-pair identity index. Incorporating region indices as explicit positional identifiers ensures that positive pairs always correspond to the same spatial location across perspectives, providing directional alignment gradients even under large viewpoint disparities.

**Dual-Pathway Functional Specialization Loss.** To drive functional separation via explicit gradient pressure rather than implicit emergence, we design two asymmetric self-supervised losses.

The *Geometric Specialization Loss*  $\mathcal{L}_{\text{geo}}$  acts exclusively on the UAV branch, using UniDepth depth maps as zero-annotation supervision. A pairwise ranking hinge loss constrains dorsal-pathway BEV feature magnitudes to be consistent with depth ordering:

$$\mathcal{L}_{\text{geo}} = \frac{1}{|\mathcal{Q}|} \sum_{(i,j) \in \mathcal{Q}} \max(0, \Delta - \text{sgn}(D_i - D_j) \cdot (\|\mathbf{f}_i\|_2 - \|\mathbf{f}_j\|_2)), \quad (11)$$

where  $\mathcal{Q}$  samples pixel pairs with  $|D_i - D_j| > 0.05$  and  $\Delta = 0.1$ . The same constraint is deliberately withheld from the satellite branch, generating asymmetric geometric gradient pressure across the two branches.

The *Inter-Stream Complementarity Loss*  $\mathcal{L}_{\text{div}}$  prevents the two branches from collapsing into redundant representations. Based on the Barlow Twins [80] cross-correlation matrix  $\mathcal{C}$  between batch-normalized embeddings  $\bar{\mathbf{e}}_s$  and  $\bar{\mathbf{e}}_d$ :

$$\mathcal{L}_{\text{div}} = \sum_c (1 - C_{cc})^2 + \lambda_{\text{off}} \sum_{c \neq c'} C_{cc'}^2, \quad (12)$$

where  $\lambda_{\text{off}} = 1.0$ . This simultaneously drives same-scene alignment (diagonal entries  $\rightarrow 1$ ) and inter-branch orthogonality (off-diagonal entries  $\rightarrow 0$ ), guaranteeing that the dual-branch design does not degenerate into single-branch redundancy.

**Total Loss** combines all signals:

$$\mathcal{L} = \mathcal{L}_{\text{lm}} + \lambda_1 \mathcal{L}_{\text{topo}} + \lambda_2 \mathcal{L}_{\text{con}} + \lambda_s (\mathcal{L}_{\text{geo}} + \mathcal{L}_{\text{div}}), \quad (13)$$

following common multi-task weighting practice [81], [82],  $\lambda_s < \lambda_1 < \lambda_2$  reflects a coarse-to-fine rationale: global contrastive alignment tolerates larger weight, regional structural alignment is moderate, and specialization losses act as light regularizers requiring the smallest weight. So we set  $\lambda_1 = 0.1$ ,  $\lambda_2 = 0.2$ ,  $\lambda_s = 0.05$ , with a 500-step warm-up for  $\mathcal{L}_{\text{geo}}$  and  $\mathcal{L}_{\text{div}}$ .

## IV. EXPERIMENTS

### A. UAV-Satellite Spatial Reasoning Benchmark

At present, despite the remarkable progress of visual language models on general scene understanding tasks, dedicated benchmarks for cross-view spatial reasoning remain scarce. Existing visual question answering datasets focus primarily on object recognition and attribute judgment from a single perspective, lacking systematic evaluation of multi-view geometric consistency, depth relationships, and topological connectivity. To address this deficiency, we develop SatAgent-SR130K, the first visual question answering dataset specifically designed for UAV-Satellite multi-view spatial reasoning (Fig. 6). Built upon GeoText-1652, the dataset encompasses 1,652 geo-referenced scenes. Each scene contains one orthographic satellite image, multiple oblique UAV images captured at varying altitudes and azimuth angles, and ground-level street view images; each image is accompanied by a global description text, a set of region-level descriptive sentences, and bounding box annotations in the normalized

format  $[c_x, c_y, w, h]$ , establishing precise correspondences between textual phrases and spatial image regions.

To fully exploit all available annotated scenes, we perform a random re-partitioning across all scenes into training, validation, and test sets at different ratios, while ensuring strict geospatial separation between the model development and final evaluation phases. Question-answer pair generation is conducted through an automated pipeline with GPT-5 Nano, employing three complementary generation strategies: (1) *bbox-grounded generation*, which uses annotated region description sentences and their bounding box coordinates as anchors to guide the LLM in generating reasoning questions grounded in specific spatial regions; (2) *caption-level generation*, which jointly inputs the global image description and all region descriptions to generate questions requiring relational reasoning across multiple annotated regions; and (3) *cross-view generation*, which simultaneously provides scene descriptions from both satellite and UAV perspectives to generate questions that can only be answered by integrating both viewpoints, such as identifying architectural structures occluded in the orthographic view but visible in the oblique view. To prevent directional semantic ambiguity arising from varying UAV shooting angles, all directional terms (left/right/up/down) are unified under the satellite image coordinate system (image left corresponds to geographic west, right to east, top to north, and bottom to south); each record is accompanied by a `direction_frame` field that annotates this convention in a machine-readable format.

To systematically evaluate cross-view spatial understanding capabilities, the designed question-answer pairs span eight predefined spatial reasoning categories: Occlusion Reasoning, Height-Footprint Consistency, Path Reachability, Vertical vs. Horizontal Separation, Depth-Order Consistency, Region Identification, Spatial Relations, and Attribute Grounding. Examples from the eight predefined spatial reasoning categories are illustrated in Fig. 6. All generated question-answer pairs undergo a three-stage quality filtering process: in the first stage, category labels are verified and automatically corrected for entries that do not conform to the standard set; in the second stage, lexical overlap scores between answer vocabulary and the vocabulary of corresponding global descriptions are computed (excluding stop words), with low-confidence answers subject to manual review to reduce the risk of hallucination; in the third stage, near-duplicate questions within the same scene are detected and only the more elaborately phrased version is retained. Furthermore, all question-answer pairs in the test set and a proportionally sampled subset of the validation set are included in a manual review queue to further ensure the quality of the evaluation data.

### B. Evaluation Metrics

We report four complementary metrics spanning lexical overlap to embedding-based semantics. **Token F1** measures order-independent bag-of-words overlap. **ROUGE-L** [83], based on the longest common subsequence, is order-sensitive. **METEOR** [84] adds stemming and WordNet synonym matching with order-aware alignment, tolerating lexical variation.

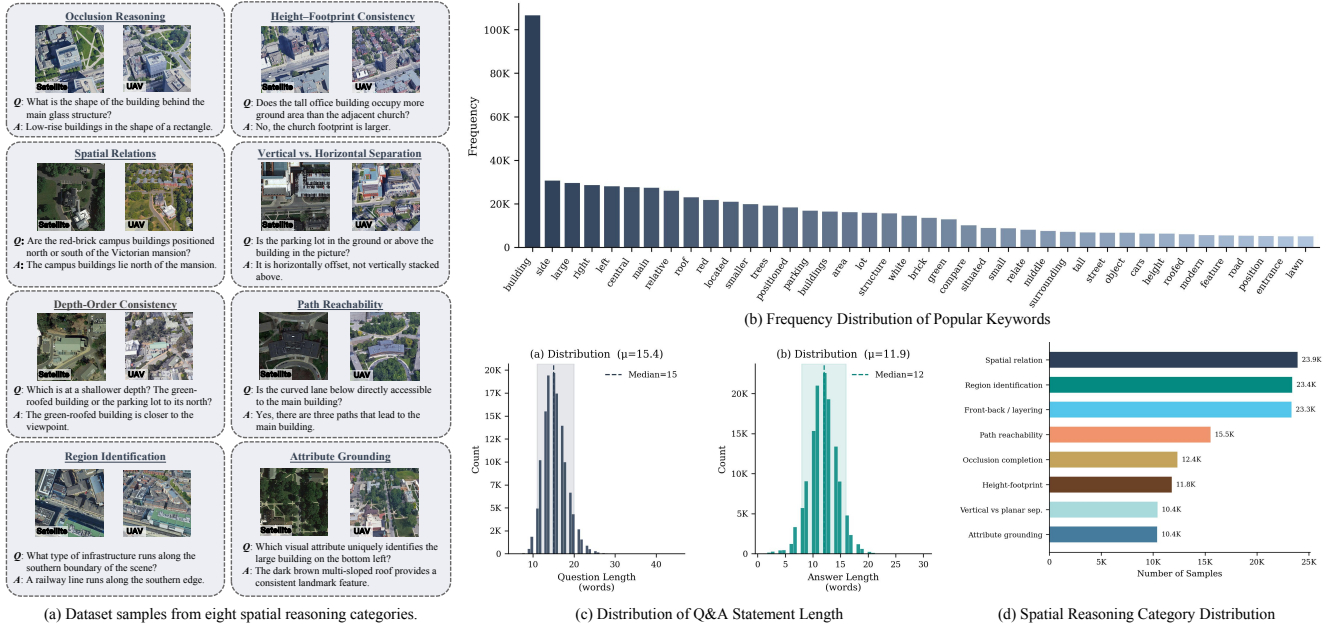


Fig. 6. Overview of the SatAgent-SR130K dataset: (a) Dataset samples from eight spatial reasoning categories; (b) vocabulary distribution; (c) length distribution of question-answer sentences; (d) distribution of eight spatial reasoning categories.

**BERTScore-F1** [85] computes contextual-embedding cosine similarity to capture semantic equivalence beyond surface form; we apply its *baseline rescaling* to counteract the anisotropy-induced compression of raw scores into a narrow high range, expanding the metric’s effective dynamic range.

Critically, all four metrics compare against the *reference answer*, not the question. A degenerate response that merely restates the question or produces fluent but non-responsive meta-commentary shares little lexical or semantic content with the factual reference, and is thus penalized across *all four* metrics: near-zero Token F1/ROUGE-L/METEOR from absent content-word overlap, and low BERTScore-F1 from the embedding distance between question restatement and concrete answer. This guards against reward hacking by fluency alone, ensuring measured gains reflect genuine answer correctness.

To assess statistical significance, we additionally compute 95% confidence intervals via bootstrap resampling (1,000 iterations) over the test set; full results are reported in Appendix C. SatAgent’s gains over the strongest baseline (SpatialRGPT, +11.69% Token F1) exceed the corresponding CI half-widths across all four metrics, confirming the improvements are statistically significant rather than sampling noise.

*C. Implementation Details*

For the parameter settings of our SatAgent method, all input images are uniformly resized and normalized, and the maximum text sequence length is set to 192 tokens. The visual encoder is CLIP ViT-B/16 [69], and the depth estimation backbone is UniDepth [70], both of which serve with their parameters frozen during training, with only the projection layer clip\_proj left trainable. The language backbone is Qwen3.5-9B, loaded in 4-bit double quantization with NF4

format; LoRA adapters are applied to its attention projection layers ( $\mathbf{W}_Q, \mathbf{W}_K, \mathbf{W}_V, \mathbf{W}_O$ ) and feed-forward network layers (gate, up, and down projections), with rank  $r=16$ , scaling factor  $\alpha_{\text{LoRA}}=32$ , and dropout rate 0.1, accounting for approximately 1% of the total parameters. During training, labels for question tokens are masked to  $-100$ , ensuring that the language modeling loss is computed only for answer tokens.

During training, we train the model for 15 epochs with an effective batch size of 16 (per-device batch size of 4 with a gradient accumulation step of 4), using the fused AdamW optimizer (adamw\_torch\_fused). The learning rate follows a cosine annealing schedule with a 200-step linear warm-up and an initial learning rate of  $1 \times 10^{-4}$ . Training employs FP16 mixed precision with TF32 acceleration enabled for matrix operations, and a gradient clipping threshold of 1.0. In the loss function, the auxiliary loss weight coefficients are set to  $\lambda_1=0.1, \lambda_2=0.2$ , and  $\lambda_s=0.05$ , tuned via the validation loss curve; evaluation is performed every 500 steps, and the checkpoint with the lowest validation loss is retained as the final model. At inference, the maximum number of newly generated tokens is set to 64, and structured prompts constrain the output format (yes/no or single-word/phrase) according to question category, eliminating the need for constrained decoding. All experiments are conducted on two NVIDIA 4090 GPUs.

*D. Comparisons with SOTA on SatAgent-SR130K*

To comprehensively evaluate SatAgent, we benchmark it against three groups of baselines on the SatAgent-SR130K test set: (i) closed-source general VLMs (GPT-5.4, Gemini-3.1-Flash-Lite-Preview, Claude-Opus-4.6, Perceptron-

TABLE II  
PERFORMANCE COMPARISON ON THE SATAGENT-SR130K TEST SET. **OVERALL** REPORTS FOUR COMPLEMENTARY METRICS (TOKEN F1, ROUGE-L, METEOR, BERTSCORE-F1); **By REASONING CATEGORY** REPORTS TOKEN F1. **BOLD**: BEST; **UNDERLINE**: SECOND BEST; CATEGORY ABBREVIATIONS — **PATH**: PATH REACHABILITY; **SPAT.**: SPATIAL RELATIONS; **ATTR.**: ATTRIBUTE GROUNDING; **REG.**: REGION IDENTIFICATION; **D.-O.**: DEPTH-ORDER CONSISTENCY; **OCC.**: OCCLUSION REASONING; **H.-F.**: HEIGHT-FOOTPRINT CONSISTENCY; **V.SEP.**: VERTICAL VS. HORIZONTAL SEPARATION

Model	Overall				By Reasoning Category							
	Token F1↑	ROUGE-L↑	METEOR↑	BERTScore-F1↑	Path	Spat.	Attr.	Reg.	D.-O.	Occ.	H.-F.	V.Sep.
<i>Closed-source General VLMs</i>												
GPT-5.4 [86]	<b>38.15</b>	<b>39.58</b>	<b>37.44</b>	<u>50.78</u>	<b>38.42</b>	<b>40.94</b>	<u>38.25</u>	<b>33.81</b>	<b>43.14</b>	<b>29.68</b>	<u>46.24</u>	<u>41.25</u>
Gemini-3.1-Flash-Lite-Preview [87]	<u>36.57</u>	<u>35.67</u>	30.45	<b>55.89</b>	34.71	<u>40.57</u>	<b>39.93</b>	<u>32.87</u>	38.52	25.75	42.33	38.98
Claude-Opus-4.6 [88]	31.70	34.65	<u>30.78</u>	45.11	27.32	35.49	22.29	28.42	33.41	23.03	36.93	33.71
Perceptron-Mk1 [89]	34.24	30.96	26.99	44.05	<u>35.53</u>	35.84	25.79	29.87	<u>39.74</u>	<u>27.41</u>	<b>50.32</b>	<b>43.09</b>
Grok-4.3 [90]	23.95	23.65	19.77	32.53	27.32	25.01	24.63	22.96	27.76	16.83	36.10	27.90
<i>Open-source General VLMs</i>												
GLM-4.5V [91]	27.86	27.04	20.85	38.12	30.90	27.85	30.53	25.81	34.81	21.23	42.75	40.73
GLM-4.6V [91]	29.75	30.57	25.44	42.11	30.00	31.19	30.78	29.31	36.32	18.39	<u>45.41</u>	<b>41.79</b>
LLaMA-3.2-90B-V [92]	<u>33.60</u>	<u>34.69</u>	31.22	40.99	30.59	<u>37.19</u>	32.71	<u>31.73</u>	33.43	24.66	35.78	34.51
Qwen3-VL-8B-Instruct [93]	32.83	34.22	<u>36.46</u>	46.02	<u>33.05</u>	34.90	<u>35.44</u>	28.62	<u>37.63</u>	<u>24.68</u>	44.58	<u>41.22</u>
MiMo-v2.5 [94]	25.89	26.79	29.22	23.20	24.06	26.66	18.24	25.97	23.04	23.78	30.28	32.19
Nemotron-Nano-Omni-30B-A3B-R. [95]	17.88	20.57	16.32	28.45	17.77	19.50	18.53	17.79	19.30	11.04	20.65	22.76
Kimi-K2.5 [96]	24.33	25.75	21.38	39.77	23.39	25.44	20.17	21.89	30.74	17.30	41.23	31.67
Step-3.7-Flash [97]	16.14	18.18	14.06	24.98	16.37	15.51	20.54	16.31	18.82	12.09	33.12	25.81
MiniMax-01 [98]	<b>39.53</b>	<b>40.62</b>	<b>39.86</b>	<b>50.15</b>	<b>37.47</b>	<b>42.51</b>	<b>39.13</b>	<b>39.22</b>	<b>42.44</b>	<b>28.23</b>	<b>52.98</b>	40.34
ERNIE-4.5-VL-424B-A47B [99]	23.50	24.39	20.76	41.00	23.16	23.92	16.79	22.64	29.95	19.28	36.59	23.57
Nex-N2-Pro [100]	26.08	28.57	25.03	40.82	26.96	27.60	24.47	24.40	28.83	20.06	34.78	28.92
Seed-2.0-Lite [101]	30.77	33.35	30.42	<u>46.53</u>	30.96	34.53	24.28	26.55	30.99	20.70	44.33	35.53
<i>Spatial-reasoning VLMs</i>												
SpaceLLaVA-1.5-7b [54]	49.66	50.01	47.65	56.66	45.54	51.23	55.33	48.89	45.63	30.33	<u>60.69</u>	<u>59.66</u>
SpatialRGPT-VILA1.5-8B [22]	<u>53.75</u>	<u>55.2</u>	<u>50.47</u>	<u>60.22</u>	<u>58.99</u>	<u>65.41</u>	<u>56.47</u>	<u>52.63</u>	<u>56.11</u>	<u>35.14</u>	49.54	55.69
<b>SatAgent (Ours)</b>	<b>65.44</b>	<b>66.10</b>	<b>62.01</b>	<b>72.31</b>	<b>65.00</b>	<b>72.45</b>	<b>62.98</b>	<b>58.90</b>	<b>70.44</b>	<b>43.54</b>	<b>78.51</b>	<b>71.70</b>

Mk1, Grok-4.3); (ii) open-source general VLMs (GLM-4.5V/4.6V, LLaMA-3.2-90B-V, Qwen3-VL-8B-Instruct, MiniMax-01, ERNIE-4.5-VL-424B-A47B, Seed-2.0-Lite, Nex-N2-Pro, etc.); and (iii) dedicated spatial-reasoning VLMs (SpaceLLaVA, SpatialRGPT). All models are evaluated zero-shot under an identical prompting protocol and inference pipeline using Token F1, ROUGE-L, METEOR, and BERTScore-F1.

As shown in Table II, SatAgent achieves an overall Token F1 of 65.44%, surpassing the previous state-of-the-art dedicated spatial reasoning model SpatialRGPT by 11.69% and the strongest general-purpose VLM MiniMax-01 by 25.91%. This gain originates from the functional differentiation of the Dual-Channel Collaborative Encoder: by explicitly separating ventral semantic processing from dorsal geometric encoding, the model simultaneously achieves global semantic understanding and local geometric perception—a combination unavailable to any existing single-perspective method.

General-purpose VLMs exhibit a characteristic semantic-strong, geometry-weak performance profile. Models such as Qwen3.5-9B and GPT-5.4 perform reasonably on categories supported by appearance-based priors (e.g., Height-Footprint Consistency) but degrade substantially on geometry-intensive tasks such as Occlusion Completion, where SatAgent leads GPT-5.4 by 13.86%. This gap directly exposes the absence of a dorsal-pathway equivalent in existing VLMs—a deficit that SatAgent’s geometry-aware 3D reconstruction encoder bridges by lifting oblique UAV features into depth-coordinated BEV

representations via 3D Gaussian soft projection.

To adapt these baselines to our cross-view evaluation protocol, SpaceLLaVA was evaluated with the drone oblique image as the sole visual input and satellite BEV context supplied via a structured system prompt. SpatialRGPT was deployed in region-free mode, replacing explicit bounding-box proposals with a full-image region token. Dedicated spatial reasoning models narrow this gap through spatial priors, yet both remain single-perspective architectures incapable of establishing cross-view topological correspondences such as path connectivity and building adjacency. SatAgent’s Multi-view Topology-Semantic Alignment Module addresses this directly, surpassing SpatialRGPT by 7.04% on Spatial Relation and 6.01% on Path Reachability. The advantage is most pronounced on cross-view reasoning tasks (55.96% vs. 46.22% for SpatialRGPT), where coordinated ventral–dorsal feedback is essential for maintaining physically consistent alignment under extreme viewpoint disparities.

#### E. Fine-Tuned VLM Baselines on SatAgent-SR130K

We compare the performance and inference cost of zero-shot and LoRA fine-tuned (FT) Qwen3.5 models (0.8B–9B) with SatAgent on the SatAgent-SR130K test set (Table III). Across all scales, fine-tuning improves Token F1 by up to 26.05%, BERTScore-F1 by up to 31.14%, indicating that domain-specific supervision substantially narrows the gap between general-purpose vision-language models and cross-view spatial reasoning. Meanwhile, simply scaling up model

TABLE III

FINE-TUNED VLM BASELINES ON SATAGENT-SR130K: ACCURACY (TOKEN F1, ROUGE-L, METEOR, BERTSCORE-F1) AND INFERENCE COST (LATENCY, THROUGHPUT, PEAK VRAM) OF ZERO-SHOT AND LoRA FINE-TUNED (FT) QWEN3.5 BACKBONES (0.8B, 2B, 4B, 9B) VERSUS SATAGENT ON SATAGENT-SR130K. **BOLD**: BEST; UNDERLINE: SECOND BEST.

Model	Accuracy				Inference Cost		
	Token F1 ↑	ROUGE-L ↑	METEOR ↑	BERTScore-F1 ↑	Latency <sub>p50</sub> (ms) ↓	Throughput (tok/s) ↑	Peak VRAM (MB) ↓
Qwen3.5-0.8B	22.77	23.37	19.87	28.49	384.9	20.3	1719
Qwen3.5-0.8B-FT	48.82	50.56	50.05	59.63	682.1	21.7	1901
Qwen3.5-2B	31.23	32.82	29.74	44.68	498.4	24.1	4302
Qwen3.5-2B-FT	48.86	50.76	50.00	60.09	701.1	20.1	4682
Qwen3.5-4B	33.65	36.18	34.93	44.97	934.8	26.4	8808
Qwen3.5-4B-FT	49.74	51.08	49.94	60.86	949.7	15.9	9488
Qwen3.5-9B	34.12	35.65	32.49	47.05	1357	15.9	17721
Qwen3.5-9B-FT	<u>50.51</u>	<u>52.43</u>	<u>50.42</u>	<u>61.91</u>	1464.5	15.6	18833
<b>SatAgent (ours)</b>	<b>65.44</b>	<b>66.10</b>	<b>62.01</b>	<b>72.31</b>	<b>1596</b>	<b>13.5</b>	<b>19056</b>

TABLE IV  
PARAMETER COUNTS OF FINE-TUNED VLM AND SATAGENT

Model	Total (M)	Trainable (M)	Trainable %
Qwen3.5-0.8B-FT	859.38	12.78	1.5
Qwen3.5-2B-FT	2224.15	21.82	0.98
Qwen3.5-4B-FT	4560.5	42.46	0.93
Qwen3.5-9B-FT	9438.9	58.20	0.62
<b>SatAgent (Ours)</b>	<b>9446</b>	<b>64.25</b>	<b>0.68</b>

size already yields diminishing marginal returns: although Qwen3.5-9B-FT has roughly 11× as many parameters as Qwen3.5-0.8B-FT, its F1 is still 14.93 % lower than that of SatAgent. We also report the inference cost of the VLM baselines and SatAgent: compared with Qwen3.5-9B, the most expensive backbone, SatAgent’s p50 latency increases by around 130 ms, throughput decreases by 2 tokens/s, and peak VRAM usage changes by around 200 MB, indicating that the additional overhead introduced by SatAgent relative to the backbone models is negligible. SatAgent achieves the best overall accuracy at an inference cost comparable to the mid-sized backbones, demonstrating that the primary driver of the performance gains is our architectural design, rather than fine-tuning or parameter scale alone. Table IV compares total and trainable parameters of the LoRA-tuned Qwen3.5 backbones (0.8B–9B) and SatAgent. All models retain trainable ratios below 1.5%. SatAgent’s total parameters (9446M) align with its Qwen3.5-9B backbone, and its trainable budget (64.25M) exceeds Qwen3.5-9B-FT (58.20M) by merely 6.05M—the architecture-specific modules beyond LoRA—indicating its performance gains stem primarily from architectural design rather than added capacity.

F. Ablation Study

To systematically validate the effectiveness of SatAgent’s design, we conduct hyperparameter analysis and three groups of progressive ablation experiments on the SatAgent-SR130K test set—analyzing the necessity of multi-view input, the key

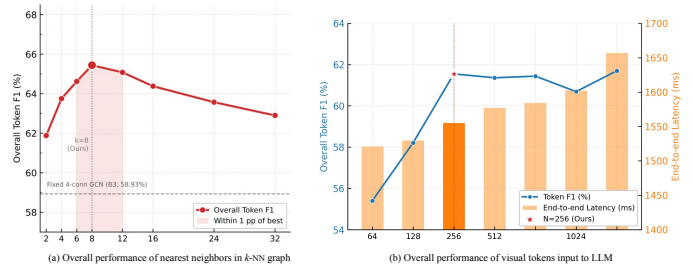


Fig. 7. Hyperparameter sensitivity analysis. (a) Effect of the number of k-NN neighbors on overall Token F1; (b) Effect of the number of visual tokens input to the LLM on Token F1.

modules of geometry-aware encoding and structural alignment, and the contribution of dual-pathway functional separation, respectively. All variants are trained independently under identical hyperparameters and training epochs, with the Overall Token F1 (%) as the primary evaluation metric. Category abbreviations follow the conventions of Table II.

Group I: Selection of Key Hyperparameters

We examine two hyperparameters that differ fundamentally in how they affect the model, and are therefore evaluated under distinct protocols, as shown in Fig. 7. The k-NN neighbor count k in the semantically adaptive topology layer only reshapes the sparse attention mask without changing the matrix-multiplication cost, primarily affecting the model’s topological modeling capacity (too small a k may omit important neighbors, while too large a k may introduce noisy connections). We therefore warm-start from the final SatAgent checkpoint; overall Token F1 peaks at k=8 and remains within 1% of the optimal value over k ∈ [6, 12], while k < 4 degrades performance sharply and k > 16 approaches the fixed four-connected GCN baseline. The visual token count N<sub>v</sub> is a structural parameter, so its value must be fixed before training the final model used in the SOTA comparison. We screen N<sub>v</sub> ∈ [64, 2048] via shortened full retraining on a training subset, and observe that N<sub>v</sub> ≥ 512 yields only marginal further gains (<1%). We ultimately adopt N<sub>v</sub>=256, which achieves the best trade-off between accuracy and inference latency.

TABLE V  
GROUP II: NECESSITY OF MULTI-VIEW INPUT. AVG.: MEAN OVER THE  
FOUR CATEGORIES SHOWN.

ID	Variant	Avg.	Path	Spat.	H.-F.	V.Sep.
A1	Drone Only	43.15	38.50	45.21	46.44	45.90
A2	Concat-2View	48.22	45.77	50.23	48.55	47.50
<b>Ours</b>	<b>SatAgent</b>	<b>71.92</b>	<b>65.00</b>	<b>72.45</b>	<b>78.51</b>	<b>71.70</b>

### Group II: Necessity of Multi-View Collaborative Input

This group validates the following core questions: whether UAV-Satellite dual-perspective collaboration is a necessary condition for reliable spatial reasoning, and whether the geometry-aware fusion scheme proposed in this paper offers substantial gains over naive feature concatenation. To this end, we retain two reference variants: **A1 (Drone Only)** zeros out the satellite branch features, leaving the model to rely solely on the UAV local perspective for reasoning, lacking global topological priors; **A2 (Concat-2View)** directly concatenates the mean-pooled CLIP global embeddings of the satellite and UAV images for input to the LLM without any BEV projection or coordinate system calibration, serving as a fair comparison baseline to evaluate the gains of the proposed geometry-aware fusion scheme.

The results are shown in Table V. The most pronounced degradation of A1 occurs in the Path Reachability category (declining by 26.50% relative to SatAgent), since path connectivity judgment requires a global topological view across regions, and the limited field of view of UAVs—constrained by flight altitude and pitch angle—cannot reliably infer from a single oblique perspective whether a path is connected across occluded regions; this result directly corroborates the irreplaceable role of the satellite top-view perspective as a global topological anchor. A2 improves over A1 by 5.07% overall, indicating that the introduction of the satellite perspective does carry effective information; however, the gap between A2 and the full model remains most pronounced in Height-Footprint Consistency (declining by 29.96%) and Vertical Separation (declining by 24.20%), which require three-dimensional spatial structure perception, indicating that directly concatenating satellite and UAV features at the semantic level fails to elicit depth and height information—explicit geometric modeling in the BEV coordinate system is a necessary prerequisite for effectively exploiting the 3D cues from the UAV perspective, and cannot be replaced by mere semantic feature superimposition.

### Group III: Key Design of Geometry-Aware BEV Encoding and Semantic Topology Alignment

This group isolates three core components of the geometry-aware encoder and the semantically adaptive topology alignment module. **B1 (w/o BEVScaleCalibrator)** removes the affine coordinate calibration module, fusing UAV BEV features with satellite features without scale/offset compensation, simulating uncorrected systematic bias between the two coordinate systems. **B2 (w/o UniDepth)** replaces the UniDepth depth backend with a lightweight CNN of comparable parameter count, isolating the impact of depth quality on BEV reconstruction. **B3 (Fixed 4-conn. GCN)** replaces the dynamic

$k$ -NN graph and multi-head attention with a standard fixed four-connected GCN, degrading the topology layer to isotropic low-pass filtering.

As shown in Table VI, each variant exhibits category-differentiated degradation that maps directly onto its module’s function. B1 degrades most on Path Reachability (−14.56%), since path-connectivity judgment depends on precise spatial correspondence between UAV BEV and satellite features, and coordinate misalignment introduces systematic displacement that disrupts cross-view topological association; Occlusion Completion, which relies more on local depth than on global alignment, declines only −5.98%, confirming that calibration benefit scales with a task’s spatial-precision demand. B2 degrades most on Height-Footprint Consistency (−14.95%) and Occlusion Completion (−7.88%), indicating that high-quality monocular depth is a prerequisite for effective 3D Gaussian reconstruction: degraded depth maps yield geometrically meaningless covariance parameters, causing the soft projection to collapse toward noise-like aggregation. B3 degrades most on Occlusion Completion (−10.78%), which requires multi-region associative reasoning, while Height-Footprint Consistency drops only −3.01%—the fixed four-connected grid aggregates only spatially adjacent nodes and cannot link semantically related but spatially non-contiguous regions (e.g., same-type buildings in different lots), quantitatively validating the advantage of the dynamic  $k$ -NN graph for semantic topological connectivity.

### Group IV: Contribution of Dual-Pathway Functional Separation

This group validates the dual-pathway functional separation design from both structural and training-signal perspectives, using Token F1 as the metric. The five variants: **C1 (Baseline, Single CLIP Stream)** removes all dual-pathway components, with both branches degraded to shared CLIP encoding; **C2 (w/o Ventral Adapter)** removes the ventral adapter, so the satellite branch degrades to standard CLIP projection without semantic prototype attention; **C3 (w/o Dorsal Adapter)** removes the dorsal adapter, so the UAV branch degrades to standard CLIP projection without geometric feature injection; **C4 (w/o Bidirectional Gating)** retains both adapters but removes cross-stream gating, processing the branches independently; **C5 (w/o Spec. Losses)** retains the full dual-pathway structure but removes  $\mathcal{L}_{\text{geo}} + \mathcal{L}_{\text{div}}$ , isolating structural from training-signal contributions.

Table VII reveals four findings. (i) *The dual-pathway architecture is necessary*: C1 lags SatAgent by 7.49%–10.35% across all categories, while C2/C3—retaining a single adapter—recover to within 3.61%–3.82%, showing the structure itself contributes independently of the specialization losses. (ii) *Category-specific degradation confirms the ventral→semantics, dorsal→geometry assignment*: despite similar overall drops, C2 degrades disproportionately on semantic tasks (Attr. −7.03%, Spat. −5.32%) while geometric tasks stay relatively intact, whereas C3 shows the inverse (H.-F. −6.66%, Occ. −6.64%, D.-O. −6.54% vs. Attr. −3.60%, Spat. −3.66%), providing direct evidence of pathway specialization. (iii) *Bidirectional gating yields consistent but modest gains*: C4 trails SatAgent uniformly by 0.93%–1.42%,

TABLE VI

GROUP III: KEY DESIGN COMPONENTS OF GEOMETRY-AWARE BEV ENCODING AND SEMANTIC TOPOLOGY ALIGNMENT. PARENTHESES DESCRIBE THE CORE DIFFERENCE BETWEEN EACH VARIANT AND THE COMPLETE MODEL. **AVG.**: MEAN OVER THE FOUR CATEGORIES SHOWN.

ID	Variant	Avg.	Path	Occ.	H.-F.	V.Sep.
B1	w/o BEVScaleCalibrator	54.41	50.44	37.56	65.88	63.77
B2	w/o UniDepth	55.53	60.45	35.66	63.56	62.43
B3	Fixed 4-conn. GCN	58.93	61.56	32.76	75.50	65.88
<b>Ours</b>	<b>SatAgent</b>	<b>64.69</b>	<b>65.00</b>	<b>43.54</b>	<b>78.51</b>	<b>71.70</b>

TABLE VII

GROUP IV: ABLATION RESULTS FOR DUAL-PATHWAY FUNCTIONAL SEPARATION. TASK ACCURACY IS MEASURED BY **TOKEN F1 (%)**. **AVG.**: MEAN OVER THE FIVE CATEGORIES SHOWN.  $\mathcal{L}_{SPEC}$  REFERS TO THE SPECIALIZATION LOSS FUNCTIONS  $\mathcal{L}_{GEO} + \mathcal{L}_{DIV}$ .

ID	Variant	Avg.	Spat.	Attr.	D.-O.	Occ.	H.-F.
C1	Baseline (Single CLIP Stream)	56.89	55.49	62.10	61.55	35.20	70.12
C2	w/o Ventral Adapter (V-Stream)	60.37	57.66	65.42	66.12	38.45	74.20
C3	w/o Dorsal Adapter (D-Stream)	60.16	59.32	68.85	63.90	36.90	71.85
C4	w/o Bidirectional Gating	64.43	62.05	71.20	69.34	42.12	77.45
C5	w/o Spec. Losses ( $\mathcal{L}_{spec}$ )	58.60	56.25	64.88	63.20	36.75	71.90
<b>Ours</b>	<b>SatAgent</b>	<b>63.98</b>	<b>72.45</b>	<b>62.98</b>	<b>70.44</b>	<b>43.54</b>	<b>78.51</b>

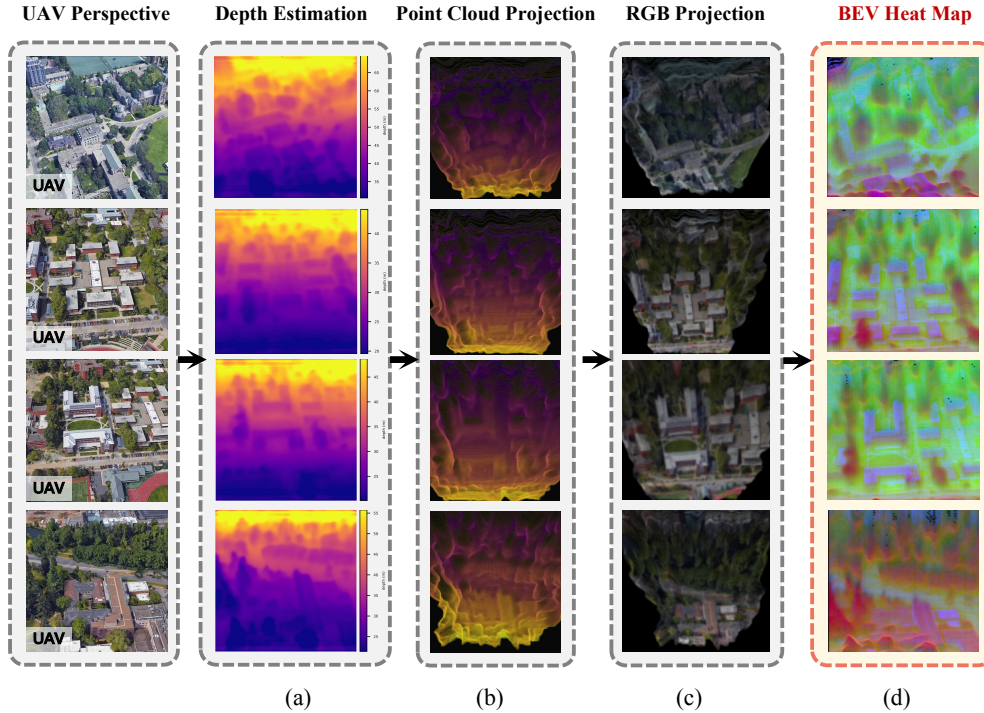


Fig. 8. Complete encoding pipeline visualization of the geometry-aware 3D reconstruction encoder: (a) per-pixel depth estimation by UniDepth; (b) 3D point cloud back-projection based on learnable camera intrinsic parameters; (c) RGB texture BEV map generated by EWA soft projection; (d) three-channel BEV feature map encoding point density (R), relative height corrected via orthographic rectification and ground-plane fitting (G), and mean brightness (B), providing a joint geometric-appearance representation for cross-view feature alignment.

consistent with its near-zero gating-strength initialization. (iv) *Specialization losses are indispensable*: C5, which keeps the dual-pathway structure but removes  $\mathcal{L}_{geo}$  and  $\mathcal{L}_{div}$ , drops 6.61%–7.57% per category—substantially more than C2 or C3 alone—confirming that explicit gradient pressure from these

losses is required to realize the full benefit of dual-pathway differentiation.

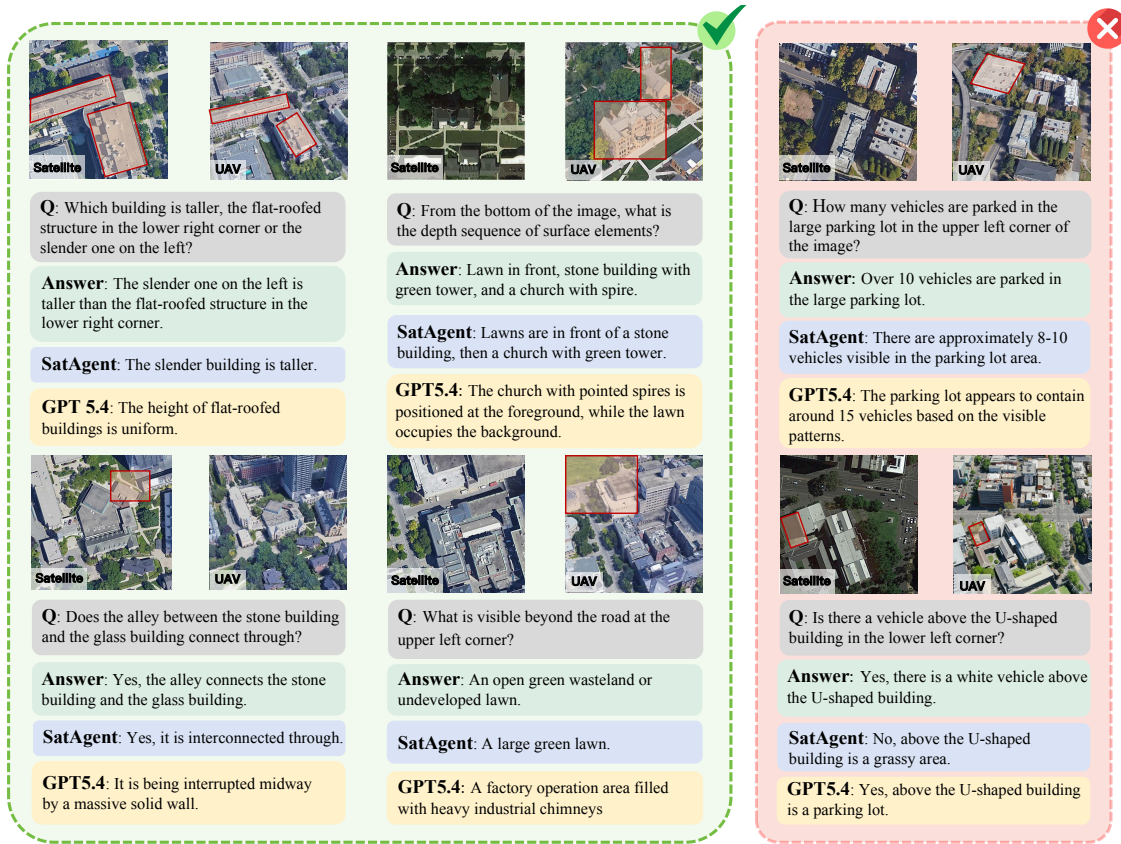


Fig. 9. Qualitative comparison of SatAgent and GPT-5.4 on 3D spatial reasoning tasks; the third column shows failure cases.

### G. Qualitative Analysis

Fig. 8 presents intermediate representation visualizations of the geometry-aware 3D reconstruction encoder across four representative scenes. Starting from UAV RGB images, the encoder estimates per-pixel absolute metric depth maps via UniDepth (column a), where clear depth discontinuities at building edges provide a reliable geometric foundation for 3D reconstruction. Pixels are then back-projected into 3D point clouds (column b) and projected onto a horizontal BEV grid with RGB texture (column c), visually approximating satellite orthographic imagery and validating the oblique-to-top-down geometric transformation. The final three-channel BEV feature map (column d) encodes point density (R), relative height (G), and mean brightness (B); perspective trapezoid distortion is eliminated via orthographic correction  $X_{ortho} = X \cdot (Z_{ref}/Z)$ , and relative height is extracted through linear ground-plane fitting  $H = Z - Z_{ground}(Y)$ , causing building rooftops to be prominently distinguished from the ground in the G channel.

Fig. 9 presents a qualitative comparison between SatAgent and GPT-5.4 across four representative spatial reasoning tasks: height-footprint consistency, depth-order consistency, path reachability, and distant region identification. In all four cases, GPT-5.4 produces geometrically implausible answers—reversing foreground-background ordering, hallucinating obstructions, or misidentifying land-cover categories at range—whereas SatAgent yields correct responses by grounding language generation on the explicit depth, height, and density

channels encoded in the BEV representation. These results demonstrate that the geometry-aware 3D reconstruction encoder confers a systematic advantage on tasks where metric spatial structure is decisive.

### H. Failure Cases and Discussion

Despite its strong overall performance, SatAgent exhibits two systematic failure modes under extreme conditions, illustrated in column three of Fig. 9.

The visual token compression required to control LLM sequence length causes spatial over-smoothing in high-density scenes, degrading fine-grained instance localization such as precise vehicle counting. When multiple instances occupy spatially adjacent BEV cells, the  $4 \times 4$  adaptive pooling merges their representations into a single token, losing the inter-instance discriminability needed for exact enumeration.

Large temporal gaps between satellite and UAV acquisitions introduce irreconcilable semantic conflicts during cross-view alignment: surface changes such as construction or vegetation growth produce feature distributions in one view that contradict the structural priors established by the other, causing cross-view gating to produce unstable fusion weights and ultimately degrading reasoning accuracy in dynamically changed areas.

Both failure modes share a common underlying tension between computational efficiency and spatial fidelity. Token compression trades representational resolution for LLM

tractability; temporal misalignment trades data acquisition flexibility for cross-view consistency. Notably, these failure modes differ qualitatively from those of single-perspective baselines such as SpatialRGPT, which degrade due to absent geometric grounding rather than resolution or temporal limitations—suggesting that SatAgent’s failures arise at a higher level of the reasoning hierarchy where multi-view collaboration is already established but fidelity constraints become binding. We plan to address these limitations in future work through adaptive token allocation conditioned on local feature entropy, and temporal-aware alignment that explicitly models surface change between acquisition timestamps.

## V. CONCLUSION

This paper proposes SatAgent, a UAV-Satellite collaborative spatial reasoning model that addresses two fundamental limitations of existing single-perspective VLMs: severe perspective distortion and the absence of explicit geometric modeling. By incorporating satellite orthographic imagery as a global structural reference alongside UAV oblique imagery, and constructing a physically grounded feature fusion pipeline—comprising dual-pathway collaborative encoding, covariance-aware 3D Gaussian BEV reconstruction, and multi-view topology-semantic alignment—SatAgent eliminates cross-view semantic misalignment within a unified metric coordinate system, endowing the LLM with spatial perception capabilities grounded in the real physical world. Evaluated on the purpose-built SatAgent-SR130K benchmark, SatAgent comprehensively surpasses existing general-purpose VLMs and dedicated spatial reasoning models across all eight reasoning categories. We plan to extend the model in future work to an “air–space–ground” tri-perspective architecture incorporating ground-level street views, explore adaptive token allocation and temporal-aware alignment to address the identified failure modes, and investigate large-scale pre-training to further improve generalization.

## REFERENCES

- [1] F. Yao, Y. Liu, W. Zhang, Z. Zhu, C. Li, N. Liu, P. Hu, Y. Yue, K. Wei, X. He *et al.*, “Aeroverse-review: Comprehensive survey on aerial embodied vision-and-language navigation,” *The Innovation Informatics*, vol. 1, no. 1, p. 100015, 2025.
- [2] F. Yao, Y. Yue, Y. Liu, Z. Wang, L. Jin, B. Zhao, J. Zhao, X. Sun, and K. Fu, “Aeroverse: Uav-agent benchmark suite for simulating, pre-training, finetuning, and evaluating aerospace embodied foundation models,” *IEEE Transactions on Pattern Analysis and Machine Intelligence*, pp. 1–18, 2026.
- [3] Y. Liu, F. Yao, Y. Yue, G. Xu, X. Sun, and K. Fu, “Navagent: Multi-scale urban street view fusion for uav embodied vision-and-language navigation,” *arXiv preprint arXiv:2411.08579*, 2024.
- [4] J. Johnson, B. Hariharan, L. Van Der Maaten, L. Fei-Fei, C. Lawrence Zitnick, and R. Girshick, “Clevr: A diagnostic dataset for compositional language and elementary visual reasoning,” in *Proceedings of the IEEE conference on computer vision and pattern recognition*, 2017, pp. 2901–2910.
- [5] P. Anderson, Q. Wu, D. Teney, J. Bruce, M. Johnson, N. Sünderhauf, I. Reid, S. Gould, and A. Van Den Hengel, “Vision-and-language navigation: Interpreting visually-grounded navigation instructions in real environments,” in *Proceedings of the IEEE conference on computer vision and pattern recognition*, 2018, pp. 3674–3683.
- [6] A. Chang, A. Dai, T. Funkhouser, M. Halber, M. Niessner, M. Savva, S. Song, A. Zeng, and Y. Zhang, “Matterport3d: Learning from rgb-d data in indoor environments,” *arXiv preprint arXiv:1709.06158*, 2017.
- [7] P. Mirowski, R. Pascanu, F. Viola, H. Soyer, A. J. Ballard, A. Banino, M. Denil, R. Goroshin, L. Sifre, K. Kavukcuoglu *et al.*, “Learning to navigate in complex environments,” *arXiv preprint arXiv:1611.03673*, 2016.
- [8] E. Kolve, R. Mottaghi, W. Han, E. VanderBilt, L. Weihs, A. Herrasti, M. Deitke, K. Ehsani, D. Gordon, Y. Zhu *et al.*, “Ai2-thor: An interactive 3d environment for visual ai,” *arXiv preprint arXiv:1712.05474*, 2017.
- [9] S. Tan, M. Ge, D. Guo, H. Liu, and F. Sun, “Knowledge-based embodied question answering,” *IEEE Transactions on Pattern Analysis and Machine Intelligence*, vol. 45, no. 10, pp. 11 948–11 960, 2023.
- [10] H. Luo, G. Lin, Y. Yao, F. Liu, Z. Liu, and Z. Tang, “Depth and video segmentation based visual attention for embodied question answering,” *IEEE Transactions on Pattern Analysis and Machine Intelligence*, vol. 45, no. 6, pp. 6807–6819, 2023.
- [11] B. Kerbl, G. Kopanas, T. Leimkühler, and G. Drettakis, “3D Gaussian splatting for real-time radiance field rendering,” *ACM Transactions on Graphics*, vol. 42, no. 4, 2023.
- [12] B. Mildenhall, P. P. Srinivasan, M. Tancik, J. T. Barron, R. Ramamoorthi, and R. Ng, “NeRF: Representing scenes as neural radiance fields for view synthesis,” in *Computer Vision – ECCV 2020*, ser. Lecture Notes in Computer Science, vol. 12346. Springer, 2020, pp. 405–421.
- [13] L. Li, Y. Zhang, Z. Jiang, Z. Wang, L. Zhang, and H. Gao, “Unmanned aerial vehicle-neural radiance field (UAV-NeRF): Learning multiview drone three-dimensional reconstruction with neural radiance field,” *Remote Sensing*, vol. 16, no. 22, p. 4168, 2024.
- [14] L. Yang, B. Kang, Z. Huang, Z. Zhao, X. Xu, J. Feng, and H. Zhao, “Depth anything V2,” in *Advances in Neural Information Processing Systems (NeurIPS)*, 2024.
- [15] S. Khose, A. Pal, A. Agarwal, Deepanshi, J. Hoffman, and P. Chatopadhyay, “SkyScenes: A synthetic dataset for aerial scene understanding,” in *Computer Vision – ECCV 2024*, ser. Lecture Notes in Computer Science, vol. 15137. Springer, 2024, pp. 19–35.
- [16] P. Yue, J. Xin, Y. Zhang, Y. Lu, and M. Shan, “Semantic-driven autonomous visual navigation for unmanned aerial vehicles,” *IEEE Transactions on Industrial Electronics*, vol. 71, no. 11, pp. 14 853–14 863, 2024.
- [17] M. Y. Arafat, M. M. Alam, and S. Moh, “Vision-based navigation techniques for unmanned aerial vehicles: Review and challenges,” *Drones*, vol. 7, no. 2, p. 89, 2023.
- [18] Y. Song, K. Shi, R. Penicka, and D. Scaramuzza, “Learning perception-aware agile flight in cluttered environments,” in *Proceedings of the IEEE International Conference on Robotics and Automation (ICRA)*, 2023, pp. 1989–1995.
- [19] M. Jia, Z. Qi, S. Zhang, W. Zhang, X. Yu, J. He, H. Wang, and L. Yi, “Omnispacial: Towards comprehensive spatial reasoning benchmark for vision language models,” *arXiv preprint arXiv:2506.03135*, 2025.
- [20] F. Liu, G. Emerson, and N. Collier, “Visual spatial reasoning,” *Transactions of the Association for Computational Linguistics*, vol. 11, pp. 635–651, 2023.
- [21] I. Stogiannidis, S. McDonagh, and S. A. Tsafaris, “Mind the gap: Benchmarking spatial reasoning in vision-language models,” *arXiv preprint arXiv:2503.19707*, 2025.
- [22] A.-C. Cheng, H. Yin, Y. Fu, Q. Guo, R. Yang, J. Kautz, X. Wang, and S. Liu, “Spatialrgpt: Grounded spatial reasoning in vision-language models,” *Advances in Neural Information Processing Systems*, vol. 37, pp. 135 062–135 093, 2024.
- [23] Y. Shi, X. Yu, L. Liu, D. Campbell, P. Koniusz, and H. Li, “Accurate 3-dof camera geo-localization via ground-to-satellite image matching,” *IEEE Transactions on Pattern Analysis and Machine Intelligence*, vol. 45, no. 3, pp. 2682–2697, 2022.
- [24] S. Chen, T. Zhu, R. Zhou, J. Zhang, S. Gao, J. C. Niebles, M. Geva, J. He, J. Wu, and M. Li, “Why is spatial reasoning hard for vlms? an attention mechanism perspective on focus areas,” *arXiv preprint arXiv:2503.01773*, 2025.
- [25] W. Zhang, W. E. Ng, L. Ma, Y. Wang, J. Zhao, A. Koenecke, B. Li, and W. Wanglu, “Sphere: Unveiling spatial blind spots in vision-language models through hierarchical evaluation,” in *Proceedings of the 63rd Annual Meeting of the Association for Computational Linguistics (Volume 1: Long Papers)*, 2025, pp. 11 591–11 609.
- [26] J. Wang, Y. Ming, Z. Shi, V. Vineet, X. Wang, S. Li, and N. Joshi, “Is a picture worth a thousand words? delving into spatial reasoning for vision language models,” *Advances in Neural Information Processing Systems*, vol. 37, pp. 75 392–75 421, 2024.

- [27] M. A. Goodale, A. D. Milner, L. S. Jakobson, and D. P. Carey, "A neurological dissociation between perceiving objects and grasping them," *Nature*, vol. 349, no. 6305, pp. 154–156, 1991.
- [28] M. A. Goodale and A. D. Milner, "Separate visual pathways for perception and action," *Trends in Neurosciences*, vol. 15, no. 1, pp. 20–25, 1992.
- [29] L. G. Ungerleider, "Two cortical visual systems," *Analysis of visual behavior*, vol. 549, pp. chapter–18, 1982.
- [30] M. Chu, Z. Zheng, W. Ji, T. Wang, and T.-S. Chua, "Towards natural language-guided drones: Geotext-1652 benchmark with spatial relation matching," in *European Conference on Computer Vision*. Springer, 2024, pp. 213–231.
- [31] J. Yang, S. Yang, A. W. Gupta, R. Han, L. Fei-Fei, and S. Xie, "Thinking in space: How multimodal large language models see, remember, and recall spaces," in *Proceedings of the IEEE/CVF Conference on Computer Vision and Pattern Recognition*, 2025. [Online]. Available: <https://arxiv.org/abs/2412.14171>
- [32] R. Li, S. Li, L. Kong, X. Yang, and J. Liang, "ViewSpatial-Bench: Evaluating multi-perspective spatial localization in vision-language models," *arXiv preprint arXiv:2505.21500*, 2025. [Online]. Available: <https://arxiv.org/abs/2505.21500>
- [33] E. Daxberger, N. Wenzel, D. Griffiths, H. Gang, J. Lazarow, G. Kohavi, K. Kang, M. Eichner, Y. Yang, A. Dehghan, and P. Gräsch, "MM-Spatial: Exploring 3D spatial understanding in multimodal LLMs," in *Proceedings of the IEEE/CVF International Conference on Computer Vision (ICCV)*, 2025, pp. 7395–7408.
- [34] S. Yang, R. Xu, Y. Xie, S. Yang, M. Li, J. Lin, C. Zhu, X. Chen, H. Duan, X. Yue *et al.*, "MMSI-Bench: A benchmark for multi-image spatial intelligence," in *International Conference on Learning Representations*, 2026. [Online]. Available: <https://arxiv.org/abs/2505.23764>
- [35] B. Zhou, H. Yang, D. Chen, J. Ye, T. Bai, J. Yu, S. Zhang, D. Lin, C. He, and W. Li, "UrbanBench: A comprehensive benchmark for evaluating large multimodal models in multi-view urban scenarios," in *Proceedings of the AAAI Conference on Artificial Intelligence*, 2025.
- [36] C.-H. Yeh, C. Wang, S. Tong, T.-Y. Cheng, Y. Zhai, Y. Chen, S. Gao, and Y. Ma, "All-angles bench: Can mlms answer different perspective questions well?" 2025.
- [37] J. Zha, Y. Fan, T. Zhang, G. Chen, Y. Chen, C. Gao, and X. Chen, "AirCOPBench: A benchmark for multi-drone collaborative embodied perception and reasoning," in *Proceedings of the AAAI Conference on Artificial Intelligence*, vol. 40, no. 2, 2026, pp. 1507–1515.
- [38] H. Xu, Y. Hu, Z. Zhu, C. Gao, Z. Wang, J. Rao, W. Lu, W. Li, Q. Yin, and Y. Li, "CityCube: Benchmarking cross-view spatial reasoning on vision-language models in urban environments," *arXiv preprint arXiv:2601.14339*, 2026. [Online]. Available: <https://arxiv.org/abs/2601.14339>
- [39] W. Zhang *et al.*, "Open3Dvqa: A benchmark for comprehensive spatial reasoning with multimodal large language model in open space," in *Proceedings of the 33rd ACM International Conference on Multimedia (ACM MM)*, 2025.
- [40] o. Li, "Uavreason: A unified, large-scale benchmark for multimodal aerial scene reasoning and generation," 2026.
- [41] D. Liu, Y. Zheng, J. Feng, G. Li, G. Shi, D. Li, and W. Dong, "Are VLMs lost between sky and space? Links<sup>2</sup>Bench for UAV-satellite dynamic cross-view spatial intelligence," *arXiv preprint arXiv:2604.02020*, 2026. [Online]. Available: <https://arxiv.org/abs/2604.02020>
- [42] H. Li, D. Li, Z. Wang, Y. Yan, H. Wu, W. Zhang, Y. Shen, W. Lu, J. Xiao, and Y. Zhuang, "Spatialladder: Progressive training for spatial reasoning in vision-language models," *arXiv preprint arXiv:2510.08531*, 2025.
- [43] C. M. Islam, O. Mamo, S. J. Chacko, X. Liu, and W. Yu, "Spatial-vilt: Enhancing visual spatial reasoning through multi-task learning," in *International Symposium on Visual Computing*. Springer, 2025, pp. 47–58.
- [44] Y. Tang, A. Qu, Z. Wang, D. Zhuang, Z. Wu, W. Ma, S. Wang, Y. Zheng, Z. Zhao, and J. Zhao, "Sparkle: Mastering basic spatial capabilities in vision language models elicits generalization to spatial reasoning," *Findings of the Association for Computational Linguistics: EMNLP*, vol. 2025, pp. 4083–4103, 2025.
- [45] Y.-H. Liao, R. Mahmood, S. Fidler, and D. Acuna, "Reasoning paths with reference objects elicit quantitative spatial reasoning in large vision-language models," in *Proceedings of the 2024 Conference on Empirical Methods in Natural Language Processing*, 2024, pp. 17028–17047.
- [46] Y. Hong, H. Zhen, P. Chen, S. Zheng, Y. Du, Z. Chen, and C. Gan, "3D-LLM: Injecting the 3D world into large language models," in *Advances in Neural Information Processing Systems (NeurIPS)*, 2023.
- [47] C. Zhu, T. Wang, W. Zhang, J. Pang, and X. Liu, "LLaVA-3D: A simple yet effective pathway to empowering LMMs with 3D-awareness," in *Proceedings of the IEEE/CVF International Conference on Computer Vision (ICCV)*, 2025.
- [48] Q. Gu, A. Kuwajerwala, S. Morin, K. M. Jatavallabhula, B. Sen, A. Agarwal, C. Rivera, W. Paul, K. Ellis, R. Chellappa, C. Gan, C. M. de Melo, J. B. Tenenbaum, A. Torralba, F. Shkurti, and L. Paull, "ConceptGraphs: Open-vocabulary 3D scene graphs for perception and planning," in *Proceedings of the IEEE International Conference on Robotics and Automation (ICRA)*, 2024, pp. 5021–5028.
- [49] Z. Peng, W. Wang, L. Dong, Y. Hao, S. Huang, S. Ma, and F. Wei, "Kosmos-2: Grounding multimodal large language models to the world," in *International Conference on Learning Representations (ICLR)*, 2024.
- [50] K. Chen, Z. Zhang, W. Zeng, R. Zhang, F. Zhu, and R. Zhao, "Shikra: Unleashing multimodal LLM's referential dialogue magic," *arXiv preprint arXiv:2306.15195*, 2023.
- [51] H. You, H. Zhang, Z. Gan, X. Du, B. Zhang, Z. Wang, L. Cao, S.-F. Chang, and Y. Yang, "Ferret: Refer and ground anything anywhere at any granularity," in *International Conference on Learning Representations (ICLR)*, 2024.
- [52] Q. Guo, S. De Mello, H. Yin, W. Byeon, K. C. Cheung, Y. Yu, P. Luo, and S. Liu, "RegionGPT: Towards region understanding vision language model," in *Proceedings of the IEEE/CVF Conference on Computer Vision and Pattern Recognition (CVPR)*, 2024, pp. 13796–13806.
- [53] Y. Yuan, W. Li, J. Liu, D. Tang, X. Luo, C. Qin, L. Zhang, and J. Zhu, "Osprey: Pixel understanding with visual instruction tuning," in *Proceedings of the IEEE/CVF Conference on Computer Vision and Pattern Recognition (CVPR)*, 2024, pp. 28202–28211.
- [54] B. Chen, Z. Xu, S. Kirmani, B. Ichter, D. Sadigh, L. Guibas, and F. Xia, "SpatialVLM: Endowing vision-language models with spatial reasoning capabilities," in *Proceedings of the IEEE/CVF Conference on Computer Vision and Pattern Recognition*, 2024, pp. 14455–14465.
- [55] P. Tian, Z. Wang, P. Cheng *et al.*, "Ucdnet: Multi-uav collaborative 3-d object detection network by reliable feature mapping," *IEEE Transactions on Geoscience and Remote Sensing*, vol. 63, pp. 1–16, 2024.
- [56] Z. Wang, P. Cheng, M. Chen *et al.*, "Drones help drones: A collaborative framework for multi-drone object trajectory prediction and beyond," in *Advances in Neural Information Processing Systems*, vol. 37, 2024, pp. 64604–64628.
- [57] D. Jiang, X. He, H. Zeng, C. Wei, M. W. Ku, Q. Liu, and W. Chen, "MANTIS: Interleaved multi-image instruction tuning," *Transactions on Machine Learning Research (TMLR)*, 2024.
- [58] F. Li, R. Zhang, H. Zhang, Y. Zhang, B. Li, W. Li, Z. Ma, and C. Li, "LLaVA-NeXT-Interleave: Tackling multi-image, video, and 3D in large multimodal models," *arXiv preprint arXiv:2407.07895*, 2024.
- [59] D. Zheng, S. Huang, and L. Wang, "Video-3D LLM: Learning position-aware video representation for 3D scene understanding," in *Proceedings of the IEEE/CVF Conference on Computer Vision and Pattern Recognition (CVPR)*, 2025.
- [60] Z. Li, W. Wang, H. Li, E. Xie, C. Sima, T. Lu, Y. Qiao, and J. Dai, "BEVFormer: Learning bird's-eye-view representation from LiDAR-camera via spatiotemporal transformers," *IEEE Transactions on Pattern Analysis and Machine Intelligence*, vol. 46, 2024.
- [61] S. Lobry, D. Marcos, J. Murray, and D. Tuia, "RSVQA: Visual question answering for remote sensing data," in *IEEE Transactions on Geoscience and Remote Sensing*, vol. 58, no. 12, 2020, pp. 8555–8566.
- [62] Y. Zhan, Z. Yuan, B. Xiong, J. Su, Q. Wang, J. Gui, R. Wang, K. Wang, and X. X. Zhu, "Rsvq: Exploring data and models for visual grounding on remote sensing data," in *ISPRS Journal of Photogrammetry and Remote Sensing*, vol. 196, 2023, pp. 89–101.
- [63] K. Wang, R. Wang, J. Zhao, J. Guo, B. Dang, Y. Zhang, and S. Xiang, "EarthVQA: Towards queryable earth via relational reasoning-based remote sensing visual question answering," in *Proceedings of the AAAI Conference on Artificial Intelligence*, vol. 38, 2024, pp. 6258–6266.
- [64] Y. Li, J. Luo, Y. Zhang, Y. Tan, J.-G. Yu, and S. Bai, "STAR: A first-ever dataset and a large-scale benchmark for scene graph generation in large-size satellite imagery," *IEEE Transactions on Pattern Analysis and Machine Intelligence*, 2024.
- [65] F. Liu, D. Chen, Z. Guan, X. Zhou, J. Zhu, Q. Ye, L. Fu, and J. Zhou, "RemoteCLIP: A vision language foundation model for remote

- sensing,” *IEEE Transactions on Geoscience and Remote Sensing*, vol. 62, pp. 1–16, 2024.
- [66] K. Kuckreja, M. S. Danish, M. Naseer, A. Das, S. Khan, and F. S. Khan, “GeoChat: Grounded large vision-language model for remote sensing,” in *Proceedings of the IEEE/CVF Conference on Computer Vision and Pattern Recognition*, 2024, pp. 27 831–27 840.
- [67] Y. Zhan, B. Xiong, and Z. Yuan, “SkyEyeGPT: Unifying remote sensing vision-language tasks via instruction tuning with large language model,” *arXiv preprint arXiv:2401.09712*, 2024.
- [68] Z. Zheng, Y. Wei, and Y. Yang, “University-1652: A multi-view multi-source benchmark for drone-based geo-localization,” in *Proceedings of the ACM International Conference on Multimedia*, 2020, pp. 1395–1403.
- [69] A. Radford, J. W. Kim, C. Hallacy, A. Ramesh, G. Goh, S. Agarwal, G. Sastry, A. Askell, P. Mishkin, J. Clark *et al.*, “Learning transferable visual models from natural language supervision,” in *International Conference on Machine Learning (ICML)*, 2021, pp. 8748–8763.
- [70] L. Piccinelli, Y.-H. Yang, C. Sakaridis, M. Segù, S. Li, L. Van Gool, and F. Yu, “Unidepth: Universal monocular metric depth estimation,” in *Proceedings of the IEEE/CVF Conference on Computer Vision and Pattern Recognition (CVPR)*, 2024, pp. 10 106–10 116.
- [71] J. Hu, L. Shen, and G. Sun, “Squeeze-and-excitation networks,” in *Proceedings of the IEEE Conference on Computer Vision and Pattern Recognition (CVPR)*, 2018, pp. 7132–7141.
- [72] Z. Liu, H. Tang, A. Ammini, X. Yang, H. Mao, D. Rus, and S. Han, “BEVFusion: Multi-task multi-sensor fusion with unified BEV representation,” in *Proceedings of the IEEE/CVF International Conference on Computer Vision (ICCV)*, 2023, pp. 5795–5805.
- [73] M. Zwicker, H. Pfister, J. van Baar, and M. Gross, “Ewa volume splatting,” in *Proceedings of the 28th annual conference on Computer graphics and interactive techniques (SIGGRAPH)*, 2001, pp. 29–38.
- [74] M. Jaderberg, K. Simonyan, A. Zisserman, and K. Kavukcuoglu, “Spatial transformer networks,” in *Advances in Neural Information Processing Systems (NeurIPS)*, 2015.
- [75] A. Vaswani, N. Shazeer, N. Parmar, J. Uszkoreit, L. Jones, A. N. Gomez, Ł. Kaiser, and I. Polosukhin, “Attention is all you need,” in *Advances in Neural Information Processing Systems (NeurIPS)*, 2017, pp. 5998–6008.
- [76] P. Veličković, G. Cucurull, A. Casanova, A. Romero, P. Liò, and Y. Bengio, “Graph attention networks,” in *International Conference on Learning Representations (ICLR)*, 2018.
- [77] J. Arevalo, T. Solorio, M. Montes-y Gómez, and F. A. González, “Gated multimodal units for information fusion,” *arXiv preprint arXiv:1702.01992*, 2017. [Online]. Available: <https://arxiv.org/abs/1702.01992>
- [78] T. Dettmers, A. Pagnoni, A. Holtzman, and L. Zettlemoyer, “Qlora: Efficient finetuning of quantized llms,” in *Advances in Neural Information Processing Systems (NeurIPS)*, 2023.
- [79] A. van den Oord, Y. Li, and O. Vinyals, “Representation learning with contrastive predictive coding,” *arXiv preprint arXiv:1807.03748*, 2018.
- [80] J. Zbontar, L. Jing, I. Misra, Y. LeCun, and S. Deny, “Barlow twins: Self-supervised learning via redundancy reduction,” in *International Conference on Machine Learning (ICML)*, 2021, pp. 12 310–12 320.
- [81] Z. Chen, V. Badrinarayanan, C.-Y. Lee, and A. Rabinovich, “GradNorm: Gradient normalization for adaptive loss balancing in deep multitask networks,” in *International Conference on Machine Learning*, 2018, pp. 794–803.
- [82] A. Kendall, Y. Gal, and R. Cipolla, “Multi-task learning using uncertainty to weigh losses for scene geometry and semantics,” in *Proceedings of the IEEE Conference on Computer Vision and Pattern Recognition*, 2018, pp. 7482–7491.
- [83] C.-Y. Lin, “Rouge: A package for automatic evaluation of summaries,” in *Text Summarization Branches Out*, 2004, pp. 74–81.
- [84] S. Banerjee and A. Lavie, “Meteor: An automatic metric for mt evaluation with improved correlation with human judgments,” in *Proceedings of the ACL Workshop on Intrinsic and Extrinsic Evaluation Measures for Machine Translation and/or Summarization*, 2005, pp. 65–72.
- [85] T. Zhang, V. Kishore, F. Wu, K. Q. Weinberger, and Y. Felix, “Bertscore: Evaluating text generation with bert,” in *International Conference on Learning Representations (ICLR)*, 2020.
- [86] OpenAI, “Gpt-5.4 system card,” OpenAI, Technical Report, 2026, accessed: 2026-04-29. [Online]. Available: <https://openai.com/>
- [87] Google DeepMind, “Gemini 3.1 flash-lite model card,” <https://deepmind.google/models/model-cards/gemini-3-1-flash-lite/>, Mar. 2026, published: 3 March 2026.
- [88] Anthropic, “Introducing claude opus 4.6,” <https://www.anthropic.com/news/claude-opus-4-6>, 2026, accessed: 2026-04-29.
- [89] Perceptron AI, “Introducing Perceptron Mk1,” <https://www.perceptron.inc/blog/introducing-perceptron-mk1>, 2026, accessed: 2026-06-12.
- [90] xAI, “Grok 4,” <https://x.ai/news/grok-4>, 2026.
- [91] V. Team, W. Hong, W. Yu, X. Gu, G. Wang, G. Gan *et al.*, “Glm-4.5v and glm-4.1v-thinking: Towards versatile multimodal reasoning with scalable reinforcement learning,” *arXiv preprint*, 2025, arXiv:2507.01006.
- [92] M. AI, “LLaMA 3.2 Model Card,” Meta AI, Technical Report, 2024, accessed: 2026-04-29. [Online]. Available: [https://www.llama.com/docs/model-cards-and-prompt-formats/llama3\\_2/](https://www.llama.com/docs/model-cards-and-prompt-formats/llama3_2/)
- [93] Q. Team, “Qwen3-vl technical report,” *arXiv preprint arXiv:2511.21631*, 2025.
- [94] “Mimo-v2.5,” 2026. [Online]. Available: [\url{https://huggingface.co/collections/XiaomiMiMo/mimo-v25}](https://huggingface.co/collections/XiaomiMiMo/mimo-v25)
- [95] NVIDIA, “Nemotron 3 nano omni: Efficient and open multimodal intelligence,” 2026. [Online]. Available: <https://arxiv.org/abs/2604.24954>
- [96] K. Team, “Kimi k2.5: Visual agentic intelligence,” *arXiv preprint*, vol. arXiv:2602.02276, 2026. [Online]. Available: <https://arxiv.org/abs/2602.02276>
- [97] S. Team, “Step 3.7 flash: A production-grade agent model for enterprise scenarios,” 2025.
- [98] MiniMax, “Minimax-01: Scaling foundation models with lightning attention,” 2025. [Online]. Available: <https://arxiv.org/abs/2501.08313>
- [99] ERNIE Team, Baidu, “ERNIE 4.5 Technical Report,” Baidu, Tech. Rep., 2025. [Online]. Available: [https://yiyan.baidu.com/blog/publication/ERNIE\\_Technical\\_Report.pdf](https://yiyan.baidu.com/blog/publication/ERNIE_Technical_Report.pdf)
- [100] Nex AGI, “Nex-N2-Pro,” <https://huggingface.co/nex-agi/Nex-N2-Pro>, 2026, accessed: 2026-06-12.
- [101] ByteDance Seed Team, “Seed 2.0 Lite,” <https://seed.bytedance.com/en/seed2>, 2026, accessed: 2026-06-12.

**Wenyi Zhang** received the B.Sc. degree from Chongqing University, Chongqing, China, in 2024. He is currently a Ph.D. student with the Aerospace Information Research Institute, Chinese Academy of Sciences, Beijing, China.

**Fanglong Yao** received the Ph.D. degree from the Aerospace Information Research Institute, Chinese Academy of Sciences, Beijing, China, in 2022. He is currently an Associate Professor with the Aerospace Information Research Institute, Chinese Academy of Sciences, Beijing, China.

**Youzhi Liu** received the B.Sc. degree from Hunan University, Changsha, China, in 2022. He is currently a Ph.D. student with the Aerospace Information Research Institute, Chinese Academy of Sciences, Beijing, China.

**Peng Hu** received the B.Sc. degree from Beihang University, Beijing, China, in 2019. He is currently a Ph.D. student with the School of Computer Science and Engineering, Beihang University, Beijing, China.

**Zhengqiu Zhu** received the Ph.D. degree in management science and engineering from the National University of Defense Technology, Changsha, China, in 2023. He is currently an Associate Professor with the College of Systems Engineering, National University of Defense Technology, Changsha, China.

**Chen Gao** received the B.Sc. and Ph.D. degrees from the Department of Electronic Engineering, Tsinghua University, Beijing, China. He is currently a Faculty Member (Research-track AP) of BNRist, Tsinghua University, Beijing, China.

**Xian Sun** received the B.Sc. degree from Beihang University (Beijing University of Aeronautics and Astronautics), Beijing, China, in 2004, and the M.Sc. and Ph.D. degrees from the Institute of Electronics, Chinese Academy of Sciences, Beijing, China, in 2009. He is currently a Professor with the Aerospace

Information Research Institute, Chinese Academy of Sciences, Beijing, China.

**Kun Fu** received the B.Sc., M.Sc., and Ph.D. degrees from the National University of Defense Technology, Changsha, China. He is currently a Professor with the Aerospace Information Research Institute, Chinese Academy of Sciences, Beijing, China.

APPENDIX A  
BASELINE MODEL DESCRIPTIONS

**GPT-5.4** [86]: OpenAI’s flagship closed-source multimodal model, used as a general-purpose reasoning baseline with strong world knowledge but limited explicit geometric grounding.

**Gemini-3.1-Flash-Lite-Preview** [87]: Google DeepMind’s lightweight multimodal model, balancing efficiency and reasoning as an efficient closed-source baseline.

**Claude-Opus-4.6** [88]: Anthropic’s high-capability multimodal model, representative of closed-source general VLMs with strong language understanding but weak metric spatial reasoning.

**Perceptron-Mk1** [89]: Perceptron AI’s vision-language model specialized for video and embodied spatial reasoning, included as a closed-source spatially-aware baseline.

**Grok-4.3** [90]: xAI’s general-purpose multimodal model, included as an additional closed-source baseline for broad comparison on spatial tasks.

**GLM-4.5V / GLM-4.6V** [91]: Zhipu AI’s open-source vision-language model series, representing mainstream Chinese open-weight multimodal baselines with general visual understanding.

**LLaMA-3.2-90B-V** [92]: Meta’s large open-source multimodal model, providing a strong general-purpose open-weight baseline for visual reasoning.

**Qwen3-VL-8B-Instruct** [93]: Alibaba’s instruction-tuned open-source vision-language model, representing a compact, efficient open-weight multimodal baseline.

**MiMo-v2.5** [94]: Xiaomi’s open-source multimodal model, included as an additional general-purpose open-weight baseline.

**Nemotron-Nano-Omni-30B-A3B-R.** [95]: NVIDIA’s compact omni-modal MoE model, evaluated as an efficient open-source baseline with reasoning-oriented post-training.

**Kimi-K2.5** [96]: Moonshot AI’s open-source multimodal model, providing a general-purpose open-weight baseline for visual-language reasoning.

**Step-3.7-Flash** [97]: StepFun’s lightweight open-source multimodal model, included as an efficiency-oriented open-weight baseline.

**MiniMax-01** [98]: MiniMax’s open-source multimodal model with long-context support, serving as a strong general-purpose open-weight baseline.

**ERNIE-4.5-VL-424B-A47B** [99]: Baidu’s large-scale MoE multimodal model, representing a heavyweight open-source baseline with heterogeneous text–vision expert routing.

**Nex-N2-Pro** [100]: Nex AGI’s MoE model post-trained from Qwen3.5 for agentic tasks, included as a reasoning-oriented open-source baseline.

**Seed-2.0-Lite** [101]: ByteDance’s omni-modal understanding model, evaluated as an efficient open-source baseline with unified video/image/text capability.

**SpaceLLaVA-1.5-7b** [54]: A spatial-reasoning-tuned VLM built on LLaVA, incorporating spatial VQA data to improve 3D relation understanding from single images.

**SpatialRGPT-VILA1.5-8B** [22]: A region-aware spatial reasoning VLM that injects depth and bounding-box region tokens for fine-grained metric spatial inference.

APPENDIX B  
INTER-CATEGORY CORRELATION ANALYSIS

To examine whether the eight reasoning categories in Table II probe distinct or overlapping capabilities, we compute the  $8 \times 8$  Pearson correlation matrix of Token F1 scores across all 20 evaluated models (19 baselines plus SatAgent), treating each model’s per-category score as one observation. Fig. 10 visualizes the resulting matrix.

Overall, correlations are uniformly high ( $r = 0.83\text{--}0.98$ ), indicating that a dominant common factor—general cross-view reasoning capability—governs performance across all categories: models that excel on one task tend to excel on most others, and vice versa. Path Reachability, Spatial Relation, and Region Identification form the most tightly coupled cluster ( $r \geq 0.97$ ), consistent with their shared reliance on global topological correspondence between the two views. Height–Footprint Consistency (H.-F.) is comparatively the most distinct category, showing the lowest correlations with Attribute Grounding ( $r = 0.83$ ), Spatial Relation ( $r = 0.84$ ), and Occlusion Completion ( $r = 0.84$ ); this category can be partially solved via appearance-based priors (e.g., building height cues from shadows or façade texture) even by models lacking explicit geometric reasoning, making it a comparatively weaker proxy for overall spatial-reasoning ability. These results support treating the eight categories as a coherent but non-redundant benchmark suite.

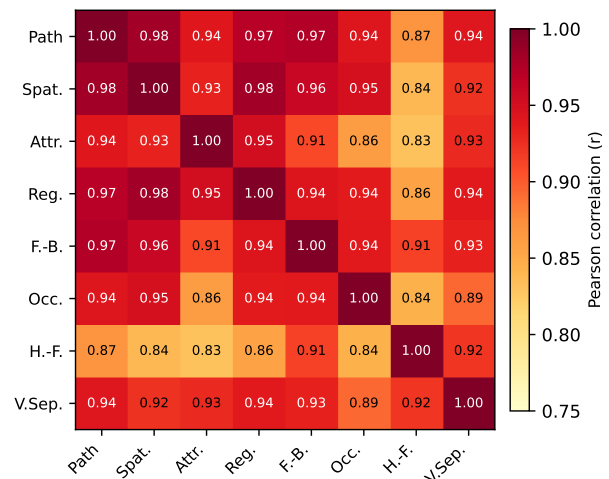


Fig. 10. Pearson correlation matrix of Token F1 scores across the eight reasoning categories in Table II, computed over 20 evaluated models (19 baselines + SatAgent).

APPENDIX C  
CONFIDENCE INTERVALS FOR TABLE II

Table VIII reports the key metrics results of Table II with 95% bootstrap confidence-interval half-widths (1,000 resamples over the test set) appended as  $\pm$  values.

TABLE VIII  
95% BOOTSTRAP CI HALF-WIDTHS (1000 RESAMPLES) FOR THE FOUR OVERALL METRICS IN TABLE II.

Model	Token F1	ROUGE-L	METEOR	BERTScore-F1
<i>Closed-source General VLMs</i>				
GPT-5.4	38.15 ± 1.35	39.58 ± 1.24	37.44 ± 1.31	50.78 ± 1.28
Gemini-3.1-Flash-Lite-Preview	36.57 ± 1.54	35.67 ± 1.61	30.45 ± 1.55	55.89 ± 1.66
Claude-Opus-4.6	31.70 ± 1.22	34.65 ± 1.14	30.78 ± 1.03	45.11 ± 1.25
Perceptron-Mk1	34.24 ± 1.66	30.96 ± 1.56	26.99 ± 1.47	44.05 ± 1.28
Grok-4.3	23.95 ± 1.17	23.65 ± 1.07	19.77 ± 0.98	32.53 ± 1.19
<i>Open-source General VLMs</i>				
GLM-4.5V	27.86 ± 1.44	27.04 ± 1.39	20.85 ± 1.47	38.12 ± 1.50
GLM-4.6V	29.75 ± 1.56	30.57 ± 1.47	25.44 ± 1.40	42.11 ± 1.50
LLaMA-3.2-90B-V	33.60 ± 1.82	34.69 ± 1.74	31.22 ± 1.52	40.99 ± 1.33
Qwen3-VL-8B-Instruct	32.83 ± 1.47	34.22 ± 1.44	36.46 ± 1.65	46.02 ± 1.29
MiMo-v2.5	25.89 ± 1.37	26.79 ± 1.41	29.22 ± 1.63	23.20 ± 1.94
Nemotron-Nano-Omni-30B-A3B-R.	17.88 ± 1.36	20.57 ± 1.34	16.32 ± 1.31	28.45 ± 1.51
Kimi-K2.5	24.33 ± 1.42	25.75 ± 1.34	21.38 ± 1.21	39.77 ± 1.39
Step-3.7-Flash	16.14 ± 1.39	18.18 ± 1.45	14.06 ± 1.31	24.98 ± 1.93
MiniMax-01	39.53 ± 1.48	40.62 ± 1.49	39.86 ± 1.60	50.15 ± 1.21
ERNIE-4.5-VL-424B-A47B	23.50 ± 1.46	24.39 ± 1.39	20.76 ± 1.35	41.00 ± 1.25
Nex-N2-Pro	26.08 ± 1.31	28.57 ± 1.14	25.03 ± 1.17	40.82 ± 1.17
Seed-2.0-Lite	30.77 ± 1.43	33.35 ± 1.34	30.42 ± 1.36	46.53 ± 1.16
<i>Spatial-reasoning VLMs</i>				
SpaceLLaVA-1.5-7b	49.66 ± 1.26	50.01 ± 1.69	47.65 ± 1.55	56.66 ± 1.47
SpatialRGPT-VILA1.5-8B	53.75 ± 1.41	55.20 ± 1.27	50.47 ± 1.53	60.22 ± 1.89
<b>SatAgent (Ours)</b>	65.44 ± 1.62	66.10 ± 1.52	62.01 ± 1.74	72.31 ± 1.42